

UC Irvine

UC Irvine Electronic Theses and Dissertations

Title

Validation of Simulated Ground Motion for the Seismic Response Assessment of Tall Building with an Application on CyberShake (15.12) Simulations Using a 40-story Steel Structure

Permalink

<https://escholarship.org/uc/item/6d86367s>

Author

Huang, Zhipeng

Publication Date

2022

Copyright Information

This work is made available under the terms of a Creative Commons Attribution-NonCommercial License, available at <https://creativecommons.org/licenses/by-nc/4.0/>

Peer reviewed|Thesis/dissertation

UNIVERSITY OF CALIFORNIA,
IRVINE

Validation of Simulated Ground Motion for the Seismic Response Assessment of Tall Building:
with an Application on CyberShake (15.12) Simulations Using a 40-story Steel Structure

THESIS

submitted in partial satisfaction of the requirements
for the degree of

MASTER OF SCIENCE

in Civil and Environmental Engineering

by

Zhipeng Huang

Thesis Committee:

Professor Farzin Zareian, Chair

Adjunct Professor Farzad Naeim

Assistant Professor of Teaching Joel Lanning

2022

TABLE OF CONTENTS

LIST OF FIGURES	iv
LIST OF TABLES	vii
ACKNOWLEDGEMENTS	viii
ABSTRACT	ix
Chapter 1 Introduction.....	1
1.1 Background	1
1.1 Ground Motion Simulation Approach.....	2
1.2 Validation Methodology	3
Chapter 2 Structural Modeling	4
2.1 Building Description	4
2.2 Modeling Properties	6
2.2.1 Floor Diaphragm.....	6
2.2.2 Lateral Mass and Gravity Load.....	7
2.2.3 Structural Framing Elements	7
2.3 OpenSees Nonlinear Pushover Curves.....	10
2.4 Building Modal Analysis	11
Chapter 3 Ground Motion Modeling	13
3.1 CyberShake (15.12) Theory	14
3.2 Ground Motion Selection and Catalogue Development Strategy	16
3.3 Modeling Idealization	16
3.4 Maximum Response - Engineering Demand Parameter (EDP).....	18
3.5 Relative Maximum Response.....	23

3.6	Verification of OpenSees Results with Modal Analysis	26
Chapter 4	Implementation of Validation Methodology	29
4.1	Overview	29
Chapter 5	Results and Discussion	33
5.1	Feature Selection	33
5.2	Variance Influence Factor	35
5.3	Regression Analysis: $\mathbf{RZZ} \rightarrow EDP$ (<i>Roof Drift Ratio, Rot100RDR</i>).....	37
5.4	Regression Analysis: $\theta \rightarrow EDP$ (<i>Roof Drift Ratio, Rot100RDR</i>).....	40
5.5	Regression Analysis: $\theta \rightarrow RZZ$ (I_{a_major}).....	44
5.6	Regression Analysis: $\theta \rightarrow RZZ$ (D_{5-95_major}).....	46
5.7	Regression Analysis: $\theta \rightarrow RZZ$ (f_{mid_major}).....	48
5.8	Additional Simulated Ground Motion Validation Result	50
Chapter 6	Summary and Conclusions	52
6.1	Summary	52
6.2	Conclusions	53
Reference	55

LIST OF FIGURES

Figure 2-1: Overview of the 40-story steel tall building with Buckling-Restrained Braced Frame System in the tower and 4 basement levels below grade in Perform-3D V8..... 5

Figure 2-2: Elevations of the main structural components in the N-S direction (left) and E-W direction (right). 8

Figure 2-3: One bay BRB framing system modeling. 9

Figure 2-4: OpenSees Pushover Analysis for the BRB framing of the tall building in both directions. 10

Figure 2-5: The natural period and mass participation regarding DOF1 and DOF3. 12

Figure 3-1: Locations of the recorded and Simulated GMs Sites. (Source: Fayaz et al., 2020).. 15

Figure 3-2: Sample of Roof Drift Ratio in time history about the major axis (Top) and the minor axis(Middle). The Square-Root-of-Sum-of-Squares of Roof Drift Ratio in time history for the major axis and the minor axis (Bottom). 19

Figure 3-3: Roof Drift Ratios comparison between MDOF model and 2DOF Model for 7 randomly selected recorded ground motions at varying degrees in one full rotation. (a) GM No.23. (b) GM No.24. (c) GM No.25. (d) GM No.28. (e) GM No.30. (f) GM No.31..... 21

Figure 3-4: Roof Drift Ratios comparison between MDOF model versus 2DOF Model for 6 randomly selected simulated ground motions at varying degrees in one full rotation. (a) Catalogue 7 GM No.75. (b) Catalogue 24 GM No.60. (c) Catalogue 59 GM No.9. (d) Catalogue 64 GM No.7. (e) Catalogue 79 GM No.168. (f) Catalogue 84 GM No.146. 22

Figure 3-5: Relations of the peak Roof Drift Ratio at each 1-degree rotation (from 0° to 179°) to the absolute maximum for the MDOF model using 12 randomly selected ground motion samples. (Left 6) Recorded ground motions. (Right 6) Simulated ground motions..... 25

Figure 3-6: The comparison of roof drift ratios obtained from 488 recorded ground motions between Modal Analysis using superposition with 10 modes and direct records from OpenSees at six selected rotational angles..... 28

Figure 5-1: Feature ranking of all **RZZ** parameters from the recorded catalogue (left) and the 23th simulated catalogue out of 51 catalogues (right). 33

Figure 5-2: Variance Inflation Factor (VIF) scores of 6 feature selected **RZZ** parameters in the recorded catalogue (top left), the simulated catalogue (bottom left), the recorded catalogue after dropping the minor components (top right), and the simulated catalogue after dropping the minor components (bottom right). 36

Figure 5-3: Regression intercept, coefficients, and RMSE for selected **RZZ** to Rot100RDR comparing the recorded catalogue to the simulated catalogues. 38

Figure 5-4: Regression intercept, coefficients, and RMSE for θ to Rot100RDR comparing the recorded catalogue to the simulated catalogues. 43

Figure 5-5: Regression intercept, coefficients, and RMSE for θ to I_{a_major} comparing the recorded catalogue to the simulated catalogues. 45

Figure 5-6: Regression intercept, coefficients, and RMSE for θ to D_{5-95_major} comparing the recorded catalogue to the simulated catalogues. 48

Figure 5-7: Regression intercept, coefficients, and RMSE for θ to f_{mid_major} comparing the recorded catalogue to the simulated catalogues. 49

Figure 5-8: The trendlines of **RZZ** Parameter and EDP (Roof Drift Ratio) Comparing the Recorded Catalogue and 51 Individual Simulated Catalogues 51

LIST OF TABLES

Table 2-1: Summary of modal properties of BRB building for two horizontal directions.....	11
Table 3-1: Ratios of Peaks at Six Selected Angles (0°, 30°, 60°, 90°, 120°, 150°) to Absolute Maximum Using an Interval of 30 Degrees.....	24
Table 5-1: The feature ranking calculated the mean of 51 simulated catalogues.....	34
Table 5-2: Summary of CB14 functional terms with the corresponding regression coefficients.	41
Table 5-3: p-value from ANOVA Using Combined Recorded and Simulated Catalogue Regression Models.....	51

ACKNOWLEDGEMENTS

I am extremely thankful to my thesis supervisor, Dr. Farzin Zareian, for his continuous guidance and enthusiasm throughout my research. Without your generous support and care, this research work will not reach this stage. Your persistence and enthusiasm have driven me to overcome several hurdles as we conducted this research. These lessons will benefit me throughout my life.

I would like to show gratitude to my committee members, Dr. Farzad Naeim and Dr. Joel Lanning, who inspired and reviewed my research work, and advised me about my professional career development.

I would also like to thank Dr. Huda Munjy of California State University, Fullerton for taking the time to help teach me the technique that can be used in my work.

A special thanks to Dr. Mohammad Javad Abdolhosseini Qomi, my undergraduate professor, for the support and encouragement when I was considering applying for master's programs.

I want to give my deepest appreciation to my parent, family, and friends for there to be supportive and helping me every step of the way.

ABSTRACT

Validation of Simulated Ground Motion for the Seismic Response Assessment of Tall Building:

with an Application on CyberShake (15.12) Simulations Using a 40-story Steel Structure

by

Zhipeng Huang

Master of Science in Civil and Environmental Engineering

University of California, Irvine, 2022

Professor Farzin Zareian, Chair

This paper evaluates the feasibility of using Cybershake (ver. 15.12) ground motions for the response assessment of a 40-story tall building. This work is the first step toward validating the use of simulated ground motions for the response assessment of tall buildings. More than 14,000 pairs of simulated ground motions from Cybershake simulation are compared against 288 pairs of earthquake records from the NGA-West2 database that occurred in the Southern California region in the past 100 years. The goal is to find the similarities between the group of simulated ground motions and the group of recorded ground motions using the engineering demand parameters (i.e., EDPs), earthquake scenarios parameters (i.e., θ), and waveform parameters (i.e., \mathbf{RZZ}) in regression models. This paper serves as the continuation of a previous work that suggested a validation methodology to investigate three relationships, $\mathbf{RZZ} \rightarrow \text{EDP}$, $\theta \rightarrow \text{EDP}$, and $\theta \rightarrow \mathbf{RZZ}$. It is observed that both recorded and simulated regression share similar features as the recorded regression coefficients fall into the population of simulated regression coefficients. Further data analysis is needed to ensure simulated ground motion is sufficient and efficient to predict the structural response.

Chapter 1 Introduction

1.1 Background

Using a nonlinear response history analysis is necessary to estimate the seismic response for the Multi-degree of freedom (MDOF) structures, especially when considering the complexity of a high-rise building with respect to several distinguishing features such as the long period at first mode of vibration, the contribution of higher modes, period elongation, and non-uniform stiffness over the building height, under dynamic earthquake loading (Jones and Zareian, 2010; Sehhati et al., 2010). Due to the effect of multiple modes on the tall building, a broad range of frequency attributes of ground motions, including both low- and high-frequency, significantly impact the estimation of structural response (Eads et al., 2016). For that matter, the seismic response analysis also requires considering historical earthquake records that are strong ground motions with large magnitudes and small site-to-source distances. However, the insufficient number of historical earthquake records which satisfy these criteria at the site of interest has been challenging for design or performance assessment. The current practice to overcome this challenge is to use ground motion selection and scaling that matches the targeted response spectrum (NIST GCR 11-917-15) to obtain recorded ground motions. The drawbacks of this approach include ignoring the effect of local geomorphic features such as the plate-edge or large crustal earthquake (Naeim F., 2001; Baker et al., 2014) and deep sedimentary basin (Baker et al., 2014), and exaggerating the scaling of Arias Intensity and the significant duration of certain selected ground motion samples; as a result, bringing bias in the unrealistic response of engineering applications (Du et al., 2019; Munjy et al., 2021). Thus, utilizing the simulated ground motion is the ideal alternative to represent both past observed records and probable future

earthquake events that may occur within the design lifetime of the structure. Therefore, ground motion simulation meets the needs of seismic response assessment for engineering applications.

1.1 Ground Motion Simulation Approach

The reliability of using simulated ground motions in engineering practice has been a major research topic over the past decade (Atkinson & Silva, 2000; Liu et al., 2006; Mena et al., 2010). The main ground motion simulation approaches include empirical function modeling, stochastic simulation, physics-based simulation, and hybrid approach simulation. Empirical function modelings are known as ground motion prediction equations (GMPEs) that are empirically calibrated using a numeric amount of existing site and source earthquake characteristics (PEER 2016/05). GMPEs are most commonly used for predicting intensity measures (e.g., peak ground acceleration [PGA], peak ground velocity [PGV], and spectral acceleration [Sa]). GMPEs provide quick access to results and demonstrate their capabilities of predictive power (Abrahamson & Silva, 2000; Kanno et al. 2006; McVerry et al., 2006; Chiou & Youngs, 2008; Akkar & Bommer, 2010; Faccioli et al., 2010; Atkinson & Boore 2011; Campbell & Bozorgnia 2014). The limitations of GMPEs are that they rely on empirical site-specific records and only produce single intensity measures. Conversely, both stochastic simulation and physics-based simulation produce synthetic accelerograms which can be used to replace earthquake records that are limited in the region. Stochastic modelings contain nonstationary characteristics in both time and frequency domains (Amin et al., 1968; Rezaeian and Kiureghian, 2008). Stochastic simulations are fast and easy to use, integrating historical earthquake source, path, and site characteristics into the simulation formation process (Atkinson & Silva 2000; Rezaeian & Sun 2014) to simulate reliable accelerograms at high frequency ($f > 1.0$ Hz).

Moreover, with the assistance of high-performance computing power in the recent decade (Cui et al., 2010), physics-based simulation modelings have gradually improved, and been less difficult to perform the complicated simulation process which synthesizes the kinematic and dynamic rupture model (Olsen et al., 2008; Schmedes, 2009), seismic wave propagation model (Graves 1996; Lee et al., 2014), and finite element method to generate synthetic ground motions at low frequency ($f < 1.0$ Hz). The hybrid simulation, particularly as CyberShake simulation, combines the stochastic simulation and physics-based simulation approach to extend broadband accelerograms (Liu et al., 2006; Graves and Pitarka, 2010; Mai et al., 2010; Star et al., 2011).

1.2 Validation Methodology

A comprehensive methodology for validating the simulated ground motions for the seismic response assessment in the bridge model is presented by Fayaz et al. (2020). It utilizes the regression equation to evaluate how similar a group of existing earthquake records is to multiple groups of ground motion obtained from CyberShake simulations. Following this similar methodology and approach for the 40-story steel building in this paper, the comparisons of regression relationships between the recorded ground motion and the simulated ground motions are made. These regression relationships consist of predicting the Engineering Demand Parameter using the important waveform parameter, the Engineering Demand Parameter using the earthquake event and site parameter, and several important waveform parameters using earthquake event and site parameters.

Chapter 2 Structural Modeling

This section examines a steel tall building model used for case studies on the seismic performance of tall buildings in the Los Angeles area (PEER 2011/05). Two models of the tall steel building were previously created in two engineering software platforms, namely Perform-3D v5 and OpenSees 2.2.1. It is noted that the stiffness of these two models differs from each other as their pushover curves are not identical. Therefore, a full inspection of the entire structures in both models is conducted. As a result, several element properties have been modified, resulting in both models' highly similar pushover curves.

Nevertheless, the clean-up version of the 40-story tall building under OpenSees 3.3.0 is used solely for this paper to collect the history of the seismic response under earthquake excitation using nonlinear time history analysis. The following discussion summarizes the modeling techniques, including structural property modeling, modeling idealization, and preliminary structural performance evaluation.

2.1 Building Description

The 40-story high-rise building rises to a total height of 544.5 ft above ground level and consists of a 40-story tower with four levels of a 227 ft by 220 ft footprint below the ground. The tower in the plan has an identical floor layout as a rectangular shape with dimensions of 170 ft by 107 ft. The Buckling-restrained Braced Frame (BRB) serves as the lateral load resistance system throughout the height of the building in both East-West (longitudinal) and North-South (transverse) directions. The framing system is symmetrical in its two principal axes. The steel structural model configuration is illustrated in Perform-3D v8.0.0., shown in Figure 2-1.

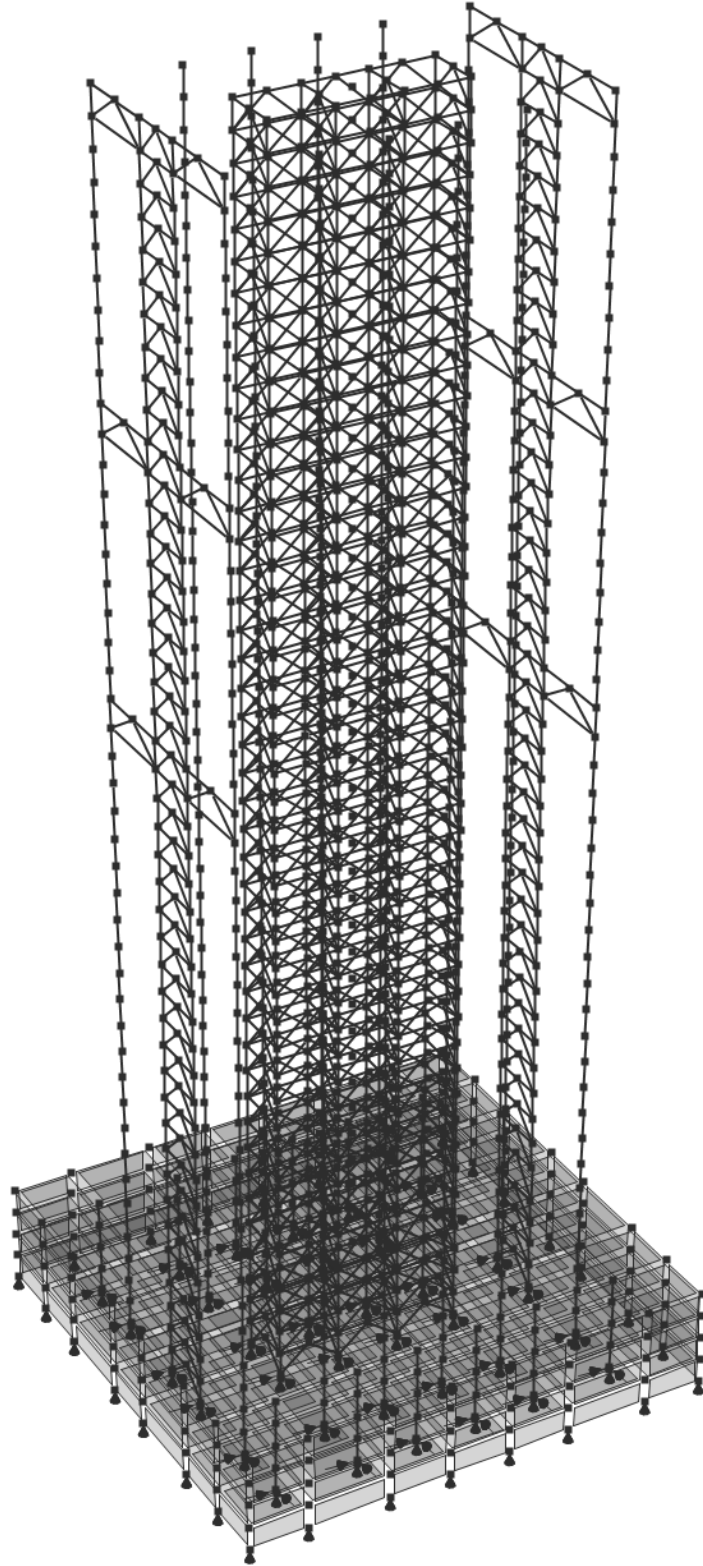


Figure 2-1: Overview of the 40-story steel tall building with Buckling-Restrained Braced Frame System in the tower and 4 basement levels below grade in Perform-3D V8

The lateral load-carrying system is replicated on each floor that contains three interior BRB bays along the E-W direction on two sides and six BRB bays along the N-S direction, spreading out from edge to edge. Additional BRB bays are only added to the N-S outriggers on the 20th, 30th, and 40th floors to strengthen the stiffness of the tall structure. The BRB system possesses the highest strength at the basement levels and progressively decreases its strength to the roof level. The tower floor and basement slabs act as rigid diaphragms to transfer inertial loads to BRB frames to basement perimeter walls at the below-grade level. The gravity load-carrying system for the tower consists of lightweight concrete-filled composite metal decking spanning between steel W-section beams and columns. The square box gravity column is made of high-strength concrete-filled steel box columns, varying from 60 in by 60 in at the base to 18 in by 18 in at the roof level. The basement structure below grade features a lightweight concrete slab floor supported by W-section gravity columns and the normal-weight concrete perimeter basement wall to retain soil pressure.

2.2 Modeling Properties

2.2.1 Floor Diaphragm

The horizontal concrete floor system in the high-rise tower is commonly used as the rigid diaphragm. As a result, all masses from floor nodes will be lumped into the master node at the center of mass. However, the current version of the solver in OpenSees is unable to complete the task on the complex tall building model due to the convergence issues encountered when using the rigid diaphragm for the floor system. An alternative solution is constructing the in-plane floor diaphragm using elastic truss elements to create a geometric triangle mesh that only connects the

column element node. The elastic materials for the truss elements are assigned a large stiffness to mimic the rigid behavior.

2.2.2 Lateral Mass and Gravity Load

The rigid diaphragm with a master node boundary constraint is incompatible with the OpenSees' solver for a complex model in this study. Thus, the lateral mass at each floor is essentially represented by a group of seismic masses assigned at different column end nodes. The seismic mass combines the dead load of self-weight plus the superimposed dead load and 25% live load. As stated in Section 2.2.1, the connectivity between floor nodes with rigid links would mimic the master node behavior. The effect of the vertical ground motion is omitted, only two horizontal (e.g., X and Z directions in OpenSees are orthogonal in the horizontal plane) seismic masses will be accelerated by the pair of bi-directional ground motions, and the remaining four degree-of-freedom with respect to one vertical mass (Y) and three rotational masses (θ_x , θ_y , and θ_z) are set to be zeros. The gravity load pattern in the vertical direction (i.e., Y direction) is imposed on the end nodes of structural elements such as column, beam, and BRB brace.

2.2.3 Structural Framing Elements

The BRB framing bay (includes the top continuous beam, two W-section columns, two diagonal braces, and four gusset plates at each end of diagonal braces) makes up most of the model skeleton and gravity columns construct a portion of the exterior perimeter. All structural elements use the beam-column element with elastic material properties to handle the linear behavior of the force and deformation, except the diagonal brace in the BRB frame, which uses

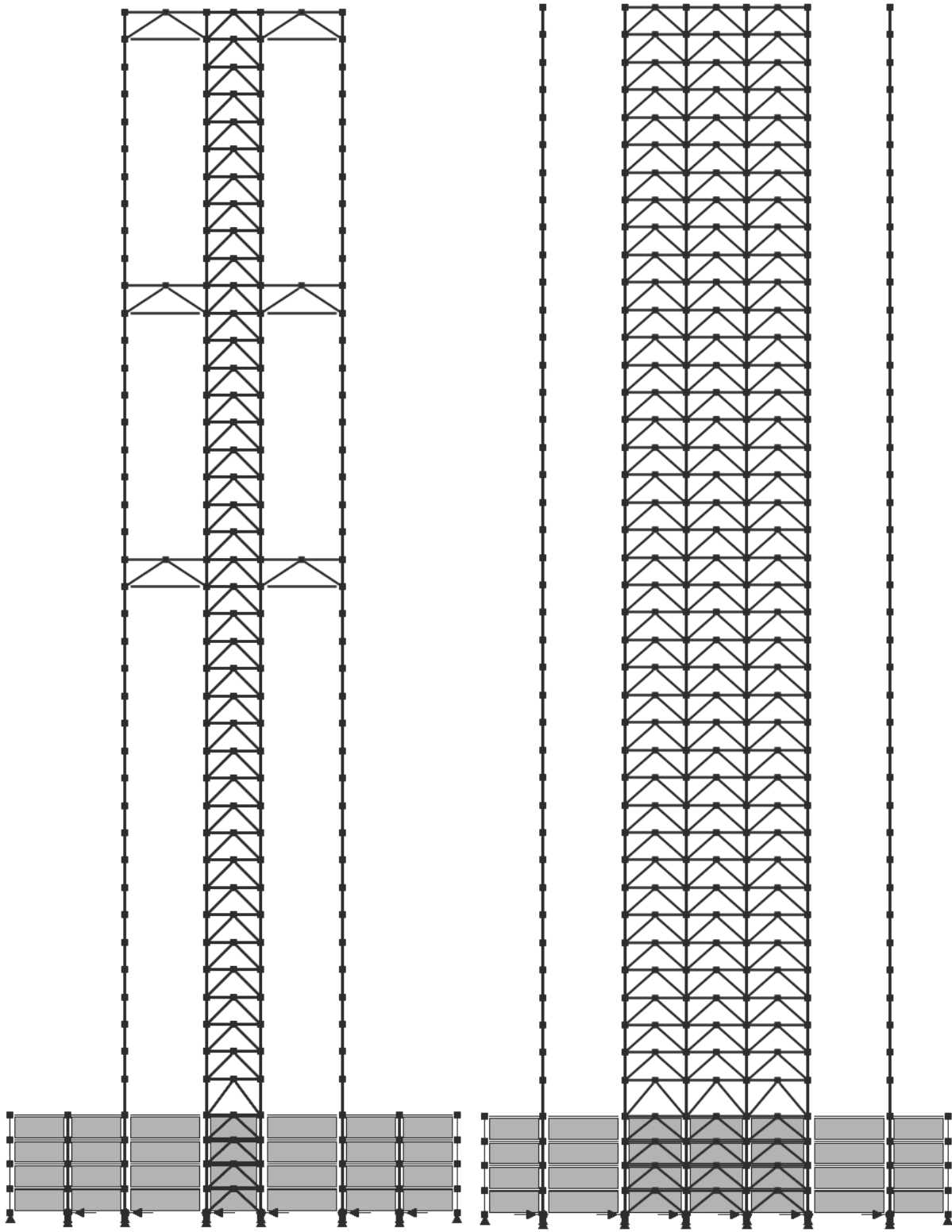


Figure 2-2: Elevations of the main structural components in the N-S direction (left) and E-W direction (right).

the truss element with the hysteretic material property to model the nonlinear behavior of the uniaxial bilinear force and deformation under the cyclic action. Figure 2-2 shows elevation views of the BRB framing system in Perform-3D V8.0.0. The perimeter wall at the basement level in the figure above is shown as the grey shell element for illustrative purposes only. The boundary condition for the perimeter nodes is assigned to be fixed.

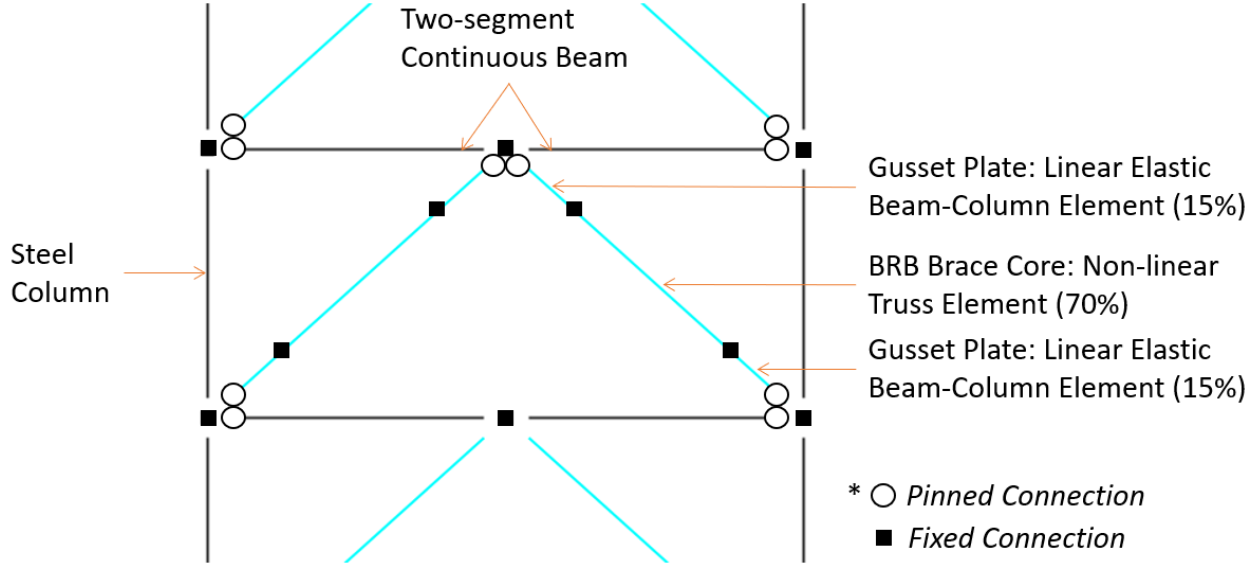


Figure 2-3: One bay BRB framing system modeling.

The continuous beam is formed by two equal-length segments of elastic steel W-section connected end to end at the top center of the BRB frame. The midpoint joint node enables the construction of the inverted BRB element model geometry. The BRB brace modeling contains three elements in series, which include two linear elements that are essentially elastic and one element capable of nonlinear action. The gusset plate is modeled with the elastic beam-column element to create the rigid end zone. Two gusset plate elements are measured as 30% (each 15%) of the diagonal length, attached to each end of the BRB brace, and assigned with a large torsional moment of inertia and second moment of inertia; thus, they are ten times stiffer than the BRB

element to prevent the undesired out-of-plane buckling from occurring. As shown in Figure 2-3, the nonlinear truss element is used to model the core of the BRB brace, which has 70% of the diagonal length, to produce the nonlinear hysteretic behavior that only resists the uniaxial deformation and cyclic loading such as tensile and compressive force. The columns are modeled using the elastic beam-column element. Both the beam-to-column and the gusset-plate-to-beam-end joint connections are imposed with the multi-point constraint to act as pins so that two nodes of each joint are allowed to deform (i.e., translational displacement and rotation) concurrently.

Lastly, the gravity columns at the tower perimeter are subject to gravity load. They are made of steel box columns filled with concrete and modeled the elastic beam-column element with modified material properties reflecting the steel and concrete composite action.

2.3 OpenSees Nonlinear Pushover Curves

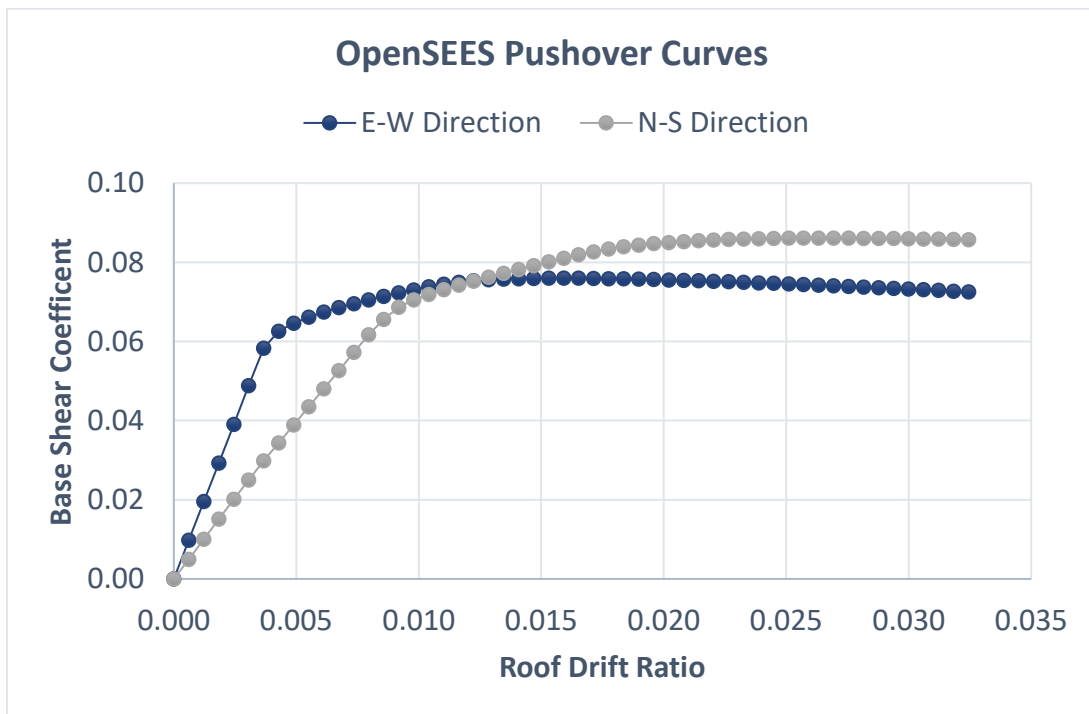


Figure 2-4: OpenSees Pushover Analysis for the BRB framing of the tall building in both directions.

The nonlinear static pushover analysis of the OpenSees model is presented in Figure 2-4. The control node at the roof corner of the structural model is forced to drift a maximum of 3% of the building height measured from the ground level to the roof. The result allows for the initial evaluation of the performance of the structural model in each principal axis. The roof drift of the model starts to yield at 0.058 and 0.062 of base shear in the E-W and N-S directions, respectively. The difference in slopes in the elastic range gives the general idea that the overall stiffness of the BRB framing building in the E-W direction is larger than the N-S direction.

2.4 Building Modal Analysis

Modal analysis for the BRB structural model aims to understand the structural dynamic properties of the building, including the natural period (denoted as T), mode shape, or mass participation (denoted as MP). The E-W and N-S orientation are specified as the degree of freedom 1 (DOF1) and the degree of freedom 3 (DOF3) correspondingly. The 3-D structural model in Figure 2-5 is constructed by the element end nodes, excluding structural elements such as beams or columns for better readability of the mode shape in the figure. Mode shape 1 to mode shape 10 are illustrated in three-dimension nodal coordinates and listed in an ascending order based on the structure's natural period. As displayed, the mass participation of the model is dominant in either of the horizontal axes due to the axisymmetric geometry. Thus, the order of modes can be rearranged based on the contribution of mass participation in each direction, as shown in Table 2-1.

Table 2-1: Summary of modal properties of BRB building for two horizontal directions.

Mode	N-S (DOF3)			E-W (DOF1)		
	1st (1)	2nd (5)	3rd (8)	1st (3)	2nd (6)	3rd (9)
Period (s)	6.03	1.71	0.84	4.44	1.46	0.79
Mass Participation (%)	66	19	6	72	15	4

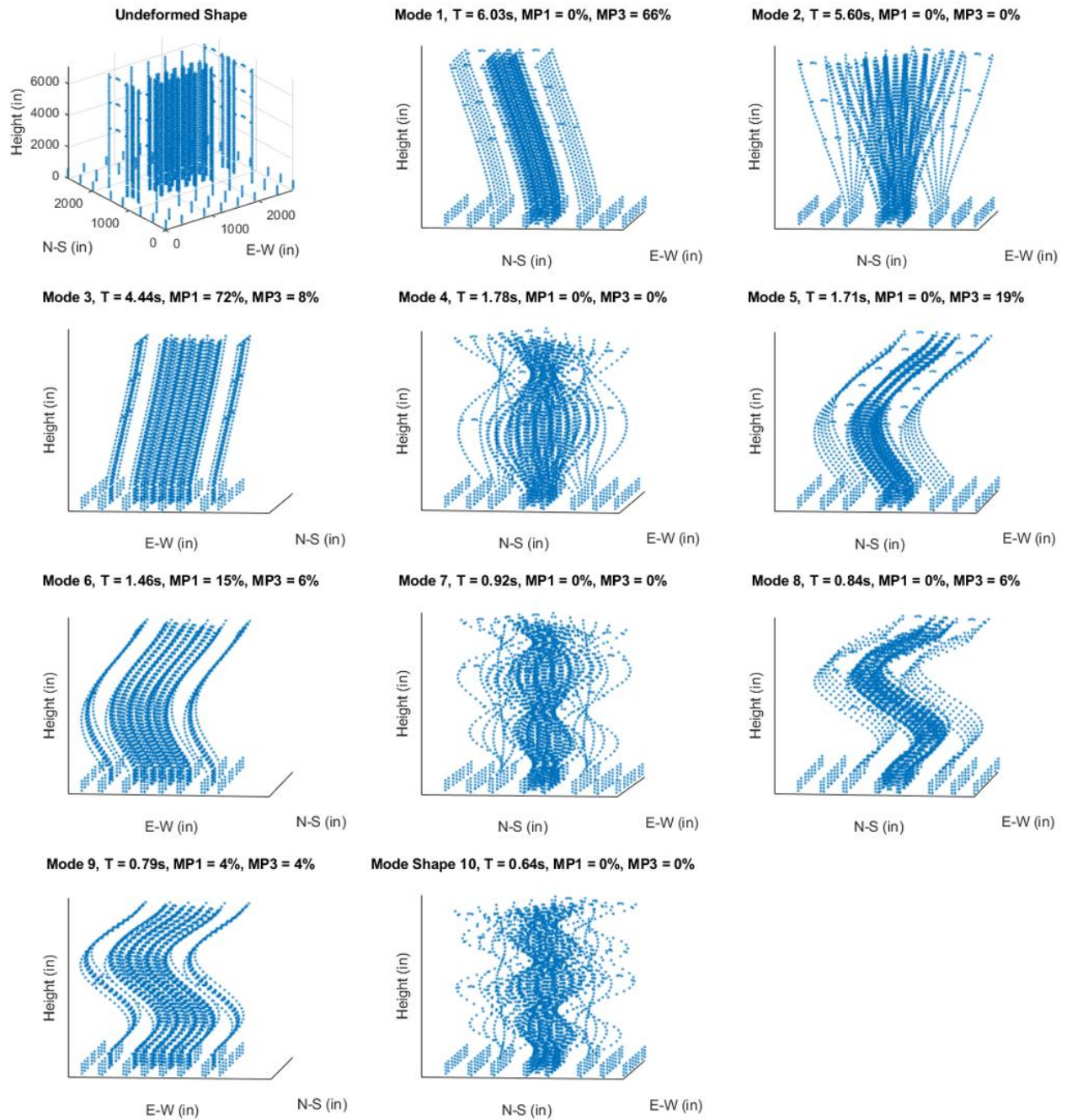


Figure 2-5: The natural period and mass participation regarding DOF1 and DOF3.

Chapter 3 Ground Motion Modeling

According to the United States Geological Survey (USGS) Earthquake Catalogue Search tool, at least ten thousand earthquake events varying in magnitude are recorded every year. Researchers and engineers are particularly interested in strong ground motions (e.g., $M_w \geq 5$) that can cause serious structural damage to tall buildings. However, the limited availability of appropriate strong ground motion records has posed a challenge for the engineering application using dynamic response history analysis in the specific location, where it will be consistent with the local earthquake characteristics. The current practice is to use ground motion selection relying on the PEER NGA database (a Next Generation Attenuation research project led by the Pacific Earthquake Engineering Research Center) to select and scale acceleration history records having similar earthquake magnitude, faulting distance, and source mechanism that match the targeted response spectrum of the application (NIST GCR 11-917-15). Although this practice is widely accepted, those selected ground motion records may misrepresent certain characteristics of acceleration waveforms in terms of strong motion duration and frequency content after scaling. To overcome this difficulty, the ground motion simulation has been continuously improved and recognized over the last decade (Zhong et al., 2017; Karimzadeh et al., 2020) to intend to substitute the recorded ground motion for the seismic response assessment. Utilizing simulated ground motion allows researchers to mitigate the shortcomings of earthquake records, such that the strong ground motion characteristics with respect to the large earthquake magnitude and site-to-source parameters in the targeted location will result in the unbiased structural response of the engineering application within the controlled design scenario (Munjy et al., 2021).

3.1 CyberShake (15.12) Theory

The simulated ground motion should be evaluated to ensure its feasibility for the engineering practice in tall building analysis. This will be done by using a statistical tool to compare the structural response to the earthquake characteristics relationship between the CyberShake ground motions and earthquake records from the NGA-West2 database. CyberShake is a physics-based ground motion simulation based on probabilistic seismic hazard analysis (PSHA), developed by the Southern California Earthquake Center (as known as SCEC) for use in Southern California (Graves et al., 2010). The simulation technique includes rupture mechanics, basin response effect, and three-dimensional wave propagation modeling. The simulated ground motions are sampled through the site-specific probabilistic seismic hazard analysis, a mixture of calculated rupture variation into the existing rupture information in the same region (specifically within and beyond 200 km of the Los Angeles region). The generation of rupture variation incorporates the hypocenter and slip distribution. Several researchers (e.g., Jordan et al., 2018; Teng and Baker, 2019; Munjy et al., 2021; Fayza et al., 2020) suggest that the CyberShake motion is sufficient for response history analysis.

This paper will utilize the CyberShake (15.12) ground motion to evaluate the structural response assessment of a tall building. The CyberShake simulation platform has been evolving and improved by a group of dedicated researchers and engineers. The most recent version is CyberShake (21.12), which focuses the study on the same region of Southern California as CyberShake (15.12); however, the main difference is that version 21.12 replaces Uniform California Earthquake Rupture Forecast Version 2.0 (UCERF2.0) with Rate-State Earthquake Simulator (denoted as RSQSim, developed by Dieterich and Richards-Dinger, 2010 & 2012) to

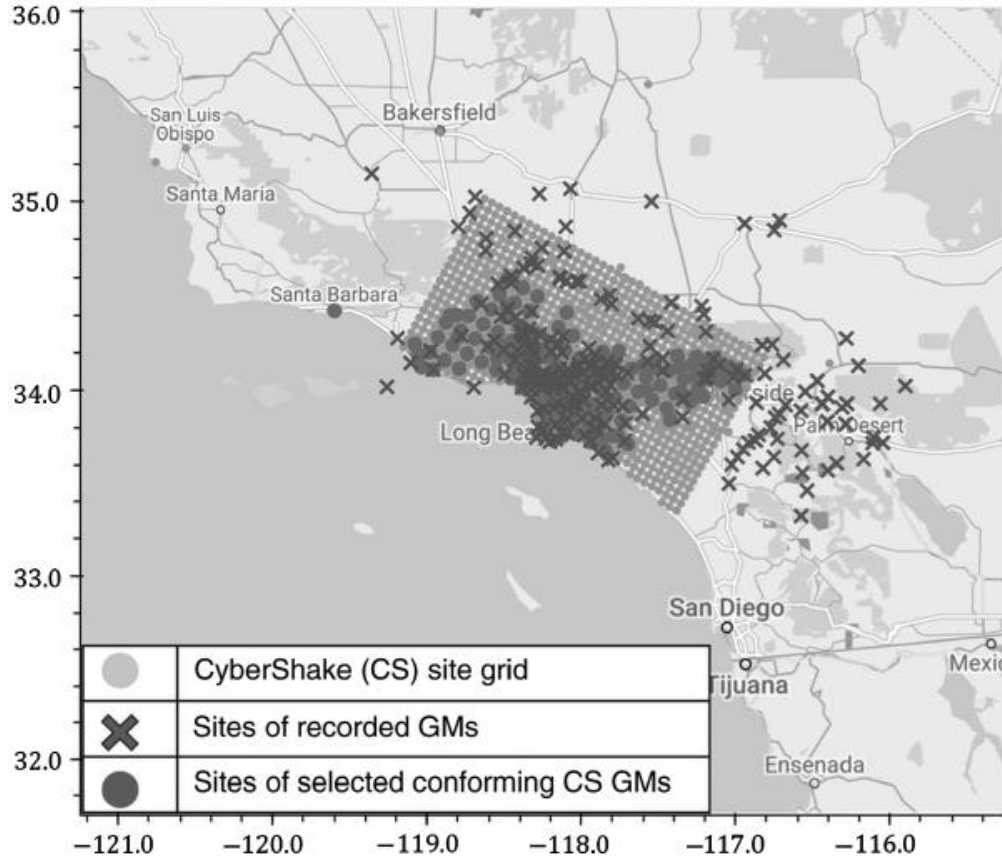


Figure 3-1: Locations of the recorded and Simulated GMs Sites. (Source: Fayaz et al., 2020)

produce the rupture variation. CyberShake (15.12) is the only available version suiting the site of interest when this study started. The other two interim updates, CyberShake (18.8) and CyberShake (17.3) study other regions, such as the Bay Area and Central California, which are not applicable for this paper. It is notable that version 15.12 has increased the number of sites to 336 (as shown in Figure 3-1) and completed the broadband feature by merging deterministic seismograms (frequency < 1.0 Hz) and stochastic seismograms (frequency > 1.0 Hz). The evaluation of simulated ground motion using a tall building structure follows the validation methodology proposed by (Fayza et al., 2020), so the CyberShake motions and the earthquake records used in this paper are identical to those in the validation methodology.

3.2 Ground Motion Selection and Catalogue Development Strategy

This section summarizes the ground motion selection and the strategy through which the catalogue of ground motions was obtained (see Fayaz et al., 2020 for detail). The simulated ground motions are generated from the CyberShake (15.12) simulation, and the recorded ground motions are selected from the NGA-West2 database. To properly compare CyberShake ground motions with earthquake records, all ground motions are chosen with magnitudes (M_w) greater than or equal to 6.0, rupture distances (R_{RUP}) less than 100 km, and time-averaged shear wave velocities in the top 30 m of the site (V_{s30}) between 200 m/s and 750 m/s. Additionally, the CyberShake simulation is confined within 100 km of the site and a span of 100 years, representing recorded earthquake activity in the region. This results in 288 pairs of recorded ground motions and 14,005 pairs of simulated ground motions.

The recorded catalogue is from earthquake scenarios in Southern California (limited as $M_w \geq 6$, $R_{RUP} \leq 100$ km, and $200 \text{ m/s} \leq V_{s30} \leq 750 \text{ m/s}$) over the period of 100 years, which is made up of 288 pairs of ground motions obtained from the NGA-West2 database. Such a real set of earthquake scenarios is compared against 51 virtual sets of earthquake scenarios, in a way to investigate the similarity between the sets. In total, 14,005 pairs of CyberShake motions are sorted into 51 simulated catalogues. These sets are obtained from Fayaz et al. (2020), applying the Monte Carlo simulation approach (Azar et al. 2019) to all possible rupture scenarios in the region.

3.3 Modeling Idealization

Given the time to complete a single response time history analysis computation varies from 5 to 60 minutes depending on the number of acceleration history steps in each ground

motion, several mitigation strategies are used in this research to ease the ultimate computational time accumulated. First, the number of simulated catalogues is reduced by half to 51 out of the original 100, which is still the minimum number of catalogues ($n > 50$) suggested in the validation methodology to conduct the comparison between the recorded and simulated catalogues, ending up with a total of 14,005 pairs of CyberShake motions for 51 catalogues. Second, considering the demanding computational time per each dynamic response history analysis (known as nonlinear time history analysis, NTHA), using the High-Performance Computing Cluster (HPC Cluster) allows for running multiple independent jobs in parallel. The high degree of computing power owing to the use of numerous CPU cores, memory storage, and GPU cores is beneficial and necessary to the end-user who performs a similar type of work. Thus, the computational effort will be significantly reduced by a factor from $\frac{1}{200}$ to $\frac{1}{1000}$, where denominators are numbers of successful runs per jobs submission depending on the traffic in the Slurm scheduler at a particular time.

3.4 Maximum Response - Engineering Demand Parameter (EDP)

The seismic structural response, or EDP, is one of the key elements in conducting the regression analysis for the validation methodology. The NTHA is used to obtain response time histories. The maximum response in all orientations of the structural model is chosen as EDP. Each orientation produces a unique response history specified for that orientation. Each resultant response history is computed using the Square Root of Sum of Squares (SRSS) of two response histories from a pair of horizontal ground motions. Therefore, the maximum resultant response can be determined through the horizontal polarization formed by peak resultant response histories in different orientations. Figure 3-2 above shows the structural model applying the nonlinear time history analysis to obtain (1) the roof drift ratio (RDR) history about the major axis (of the building) in the figure on the top, (2) the RDR history about the minor axis in the middle figure, and (3) the SRSS of RDR histories in black and the absolute maximum RDR as the black dot (Other SRSS RDR histories in cyan are plotted at other orientations using the same ground motion from earthquake records) in the figure on the bottom. The maximum roof drift ratio (denoted as Rot100RDR later) is useful to understand how similar the simulated ground motion is to comparing the recorded ground motion.

Determining the maximum response at the critical angle is challenging because the maximum response can occur in any orientation without a recognizable pattern of any intensity parameter. This paper has investigated several approaches to identify the critical angle that cause the maximum roof drift ratio. Multiple-degrees-of-freedom (MDOF) tall building model and the simplified Two-degree-of-freedom (2DOF) lollipop model are utilized, applying multiple ground motions with one full cycle of rotation. Results are drawn in the following.

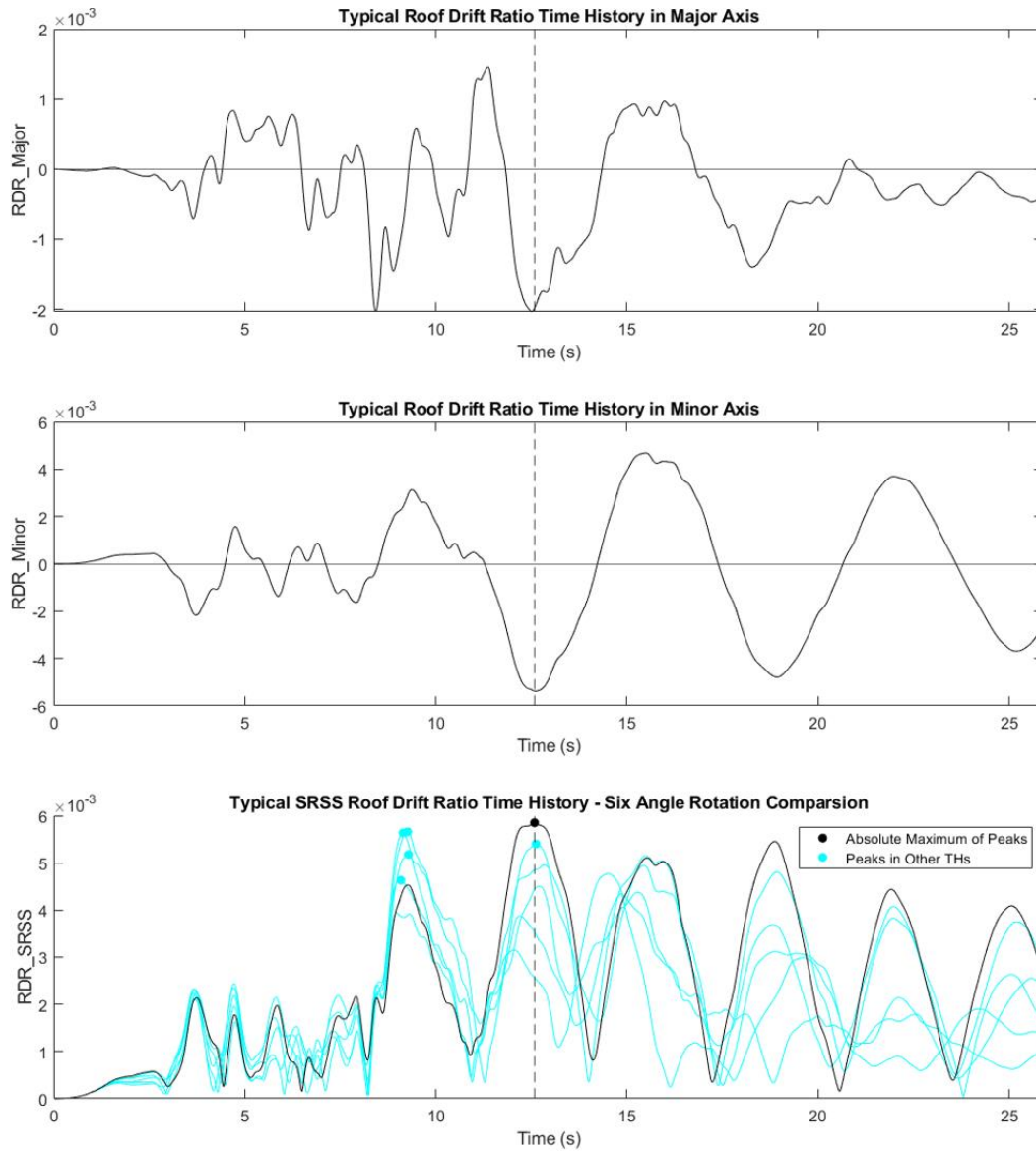
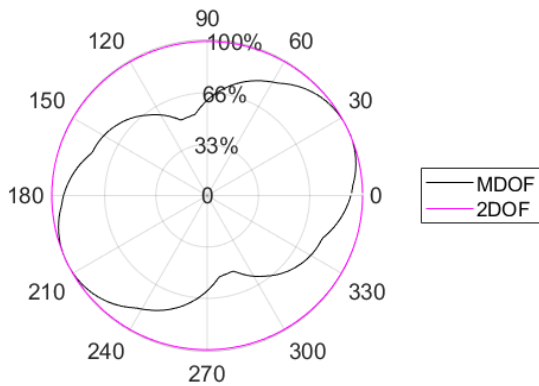


Figure 3-2: Sample of Roof Drift Ratio in time history about the major axis (Top) and the minor axis (Middle). The Square-Root-of-Sum-of-Squares of Roof Drift Ratio in time history for the major axis and the minor axis (Bottom).

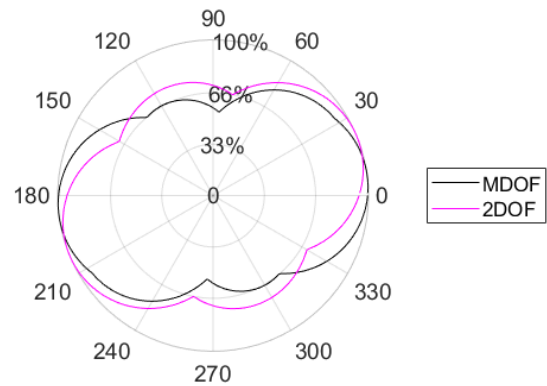
1. The corresponding rotational angle given the maximum Arias Intensity does not guarantee the maximum roof drift ratio. This has been confirmed with 12 cases of ground motion in a side study.

2. A simplified 2DOF model running response history analysis is utilized due to its simplicity. A method to predict the critical angle using near-fault ground motions is proposed by (Sebastiani et al. 2018). The simplified 2DOF model used in this section consists of 1 unit of virtual mass, 1 unit of virtual height, and the bi-directional fundamental periods as same as the MDOF model. For comparison, 12 pairs of horizontal ground motions containing 6 recorded motions and 6 simulated motions are applied to the structural model with 1-degree increments from 0 to 360 degrees. The peak RDRs are the resultant response by taking the SRSS of the pair of response histories. Figure 3-3 below illustrates the simplified 2DOF and MDOF models with varying degrees of polarization. Note that the maximum RDRs for both recorded and simulated models are scaled and normalized to the largest of these two models in percentage in the outer ring. While the purple line tends to trace the black line (MDOF-RDR) in Figure 3-4(b), the other 5 out of 6 polar plots differ. The maximum RDRs in (d) and (e) differ more than 60 degrees, indicating not all ground motions share similar MDOF and 2DOF responses. Interestingly, the results of simplified 2DOF models and MDOF models are similar in the simulated set of ground motions in Figure 3-4. The simplified 2DOF model closely predicts the critical angle to estimate the maximum RDR. However, the peak RDR of the simplified 2DOF model in all directions in Figure 3-4(b) only changes slightly as no directivity effect is exhibited during the ground motion rotation. As a result, the simplified 2DOF may not accurately predict the critical angle where the maximum RDR occurs.

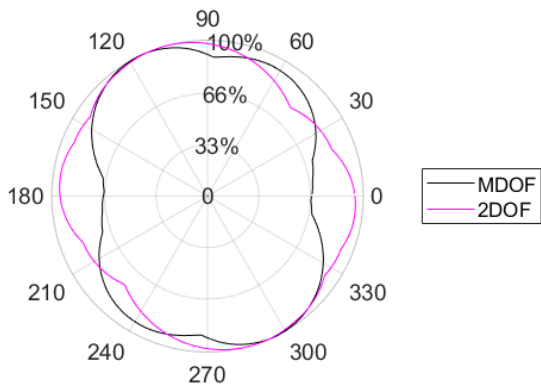
Recorded Ground Motion No.23
Scaled RDR(MDOF) vs. Scaled RDR(2DOF)



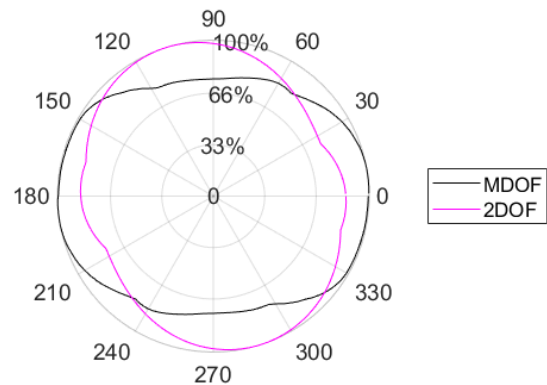
Recorded Ground Motion No.24
Scaled RDR(MDOF) vs. Scaled RDR(2DOF)



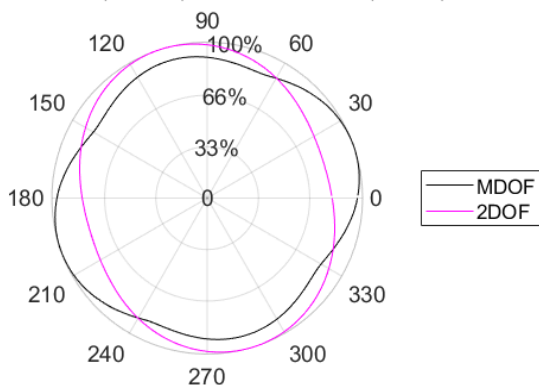
Recorded Ground Motion No.25
Scaled RDR(MDOF) vs. Scaled RDR(2DOF)



Recorded Ground Motion No.28
Scaled RDR(MDOF) vs. Scaled RDR(2DOF)



Recorded Ground Motion No.30
Scaled RDR(MDOF) vs. Scaled RDR(2DOF)



Recorded Ground Motion No.31
Scaled RDR(MDOF) vs. Scaled RDR(2DOF)

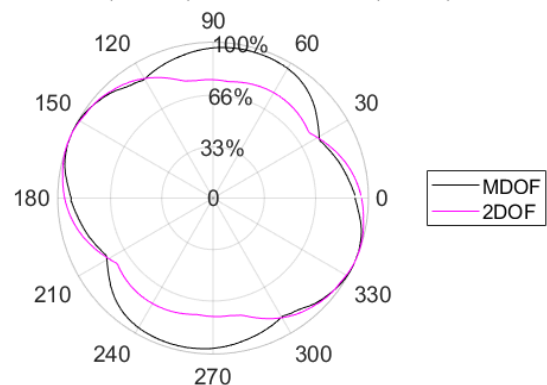
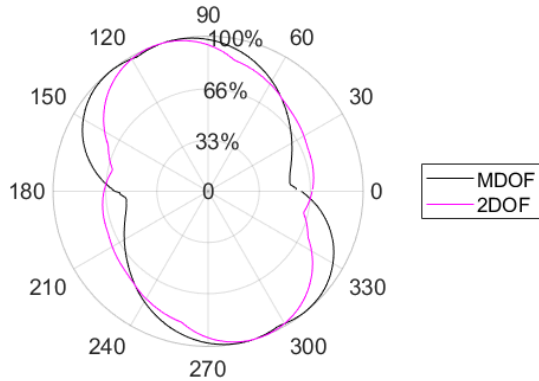
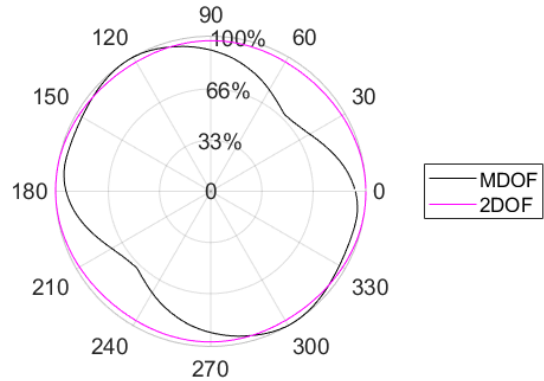


Figure 3-3: Roof Drift Ratios comparison between MDOF model and 2DOF Model for 7 randomly selected recorded ground motions at varying degrees in one full rotation. (a) GM No.23. (b) GM No.24. (c) GM No.25. (d) GM No.28. (e) GM No.30. (f) GM No.31.

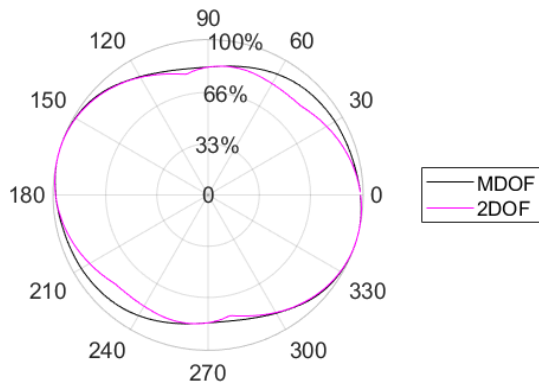
Catalog 7 Simulated Ground Motion No.75
Scaled RDR(MDOF) vs. Scaled RDR(2DOF)



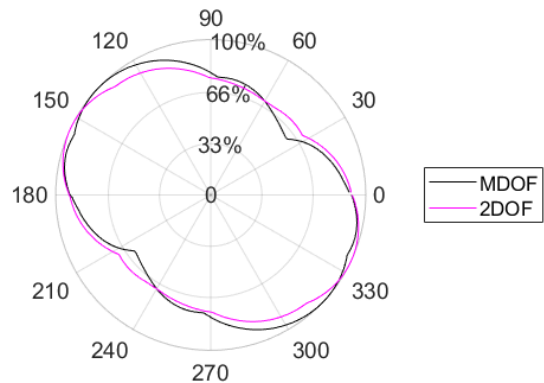
Catalog 24 Simulated Ground Motion No.60
Scaled RDR(MDOF) vs. Scaled RDR(2DOF)



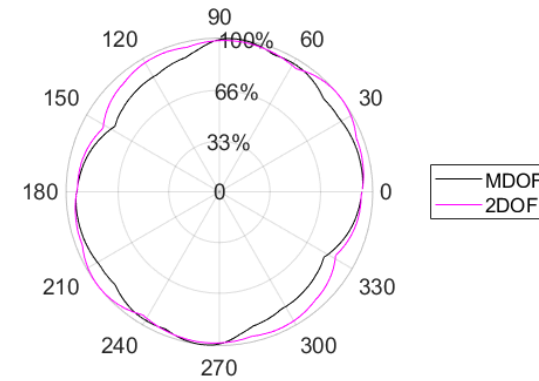
Catalog 59 Simulated Ground Motion No.9
Scaled RDR(MDOF) vs. Scaled RDR(2DOF)



Catalog 64 Simulated Ground Motion No.7
Scaled RDR(MDOF) vs. Scaled RDR(2DOF)



Catalog 79 Simulated Ground Motion No.168
Scaled RDR(MDOF) vs. Scaled RDR(2DOF)



Catalog 84 Simulated Ground Motion No.146
Scaled RDR(MDOF) vs. Scaled RDR(2DOF)

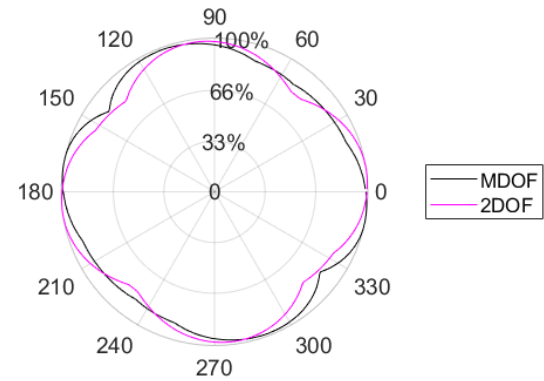


Figure 3-4: Roof Drift Ratios comparison between MDOF model versus 2DOF Model for 6 randomly selected simulated ground motions at varying degrees in one full rotation. (a) Catalogue 7 GM No.75. (b) Catalogue 24 GM No.60. (c) Catalogue 59 GM No.9. (d) Catalogue 64 GM No.7. (e) Catalogue 79 GM No.168. (f) Catalogue 84 GM No.146.

3.5 Relative Maximum Response

This part discusses the approach to obtaining Rot100RDR. Instead of changing the orientation of the building every 1 degree to find the critical angle which leads to the absolute maximum roof drift ratio, changing with a 30-degree increment is proposed in this research. We hypothesize that 30-degree increments are enough to arrive at 90% of Rot100RDR. To demonstrate this, the structural model is rotated at six selected angles (0°, 30°, 60°, 90°, 120°, and 150°). Each RDR associated with that angle is listed in Table 3-1 for 12 different ground motions. The Peak-To-Absolute-Maximum Ratio is calculated by dividing the peak of response history by Rot100RDR, which describes how much the peak of RDR with 30-degree increments can achieve Rot100RDR. The RDR highlighted in red in each ground motion is the highest RDR compared to the other five in the same ground motion. Table 3-1 shows that both recorded and simulated ground motions reach at least 98% of the absolute maximum in their particular orientations. These relatively high values of maximum RDR describe the best maximum possible response in all directions between 0 to 180 degrees.

To further explore the variation of the Peak-To-Absolute-Maximum ratio in the polarization, Rot100RDR is spotted at the crest as shown in Figure 3-5, with a 30-degree interval extended 15 degrees beyond and before the absolute maximum. Because of the axisymmetric geometry of the tall building, the maximum response will repeat by 1π radians starting at the orientation of 180 degrees. The polarized line is then horizontally depicted as the wavelike line representing rotational angles from 0 to 180 degrees. The horizontal dash line defines the threshold of the lowest ratios among those three points showing as solid black circles. The red star is the relative maximum RDR obtained by rotating the ground motion at every 30 degrees, which has been summarized in Table 3-1. It is noticeable that almost all of the relative maximum

RDRs fall inside the 30-degree interval (of the absolute maximum at the crest) with the exception of the simulated ground motion No.75 from Catalogue 7 (where it shows the absolute maximum at 120° is still higher than the threshold of 98% at 89°). For the extreme case in the simulated ground motion No.168 of Catalogue 79, the lowest Peak-To-Absolute Maximum at 93% at 99° within the 30-degree interval is observed. Despite these exceptional cases, results indicate that the 30-degree increment in the ground motion rotation can capture Rot100RDR by approximately 90 percent.

Table 3-1: Ratios of Peaks at Six Selected Angles (0°, 30°, 60°, 90°, 120°, 150°) to Absolute Maximum Using an Interval of 30 Degrees.

<i>Ground Motion Sample Index</i>	<i>Peak-To-Absolute-Maximum Ratio (Roof Drift Ratio)</i>					
	<i>0°</i>	<i>30°</i>	<i>60°</i>	<i>90°</i>	<i>120°</i>	<i>150°</i>
<i>Recorded GM023</i>	0.93	0.998	0.85	0.62	0.59	0.77
<i>Recorded GM024</i>	0.996	0.94	0.79	0.56	0.66	0.84
<i>Recorded GM025</i>	0.67	0.79	0.93	0.90	0.999	0.87
<i>Recorded GM028</i>	0.998	0.96	0.84	0.75	0.79	0.98
<i>Recorded GM030</i>	0.97	0.99	0.89	0.90	0.90	0.84
<i>Recorded GM031</i>	0.91	0.78	0.96	0.97	0.89	0.99
<i>Simulated C007 GM075</i>	0.58	0.62	0.82	0.975	0.983	0.94
<i>Simulated C024 GM060</i>	0.93	0.74	0.75	0.91	0.998	0.96
<i>Simulated C059 GM009</i>	0.982	0.95	0.90	0.82	0.87	0.987
<i>Simulated C064 GM007</i>	0.89	0.69	0.69	0.78	0.96	0.99
<i>Simulated C079 GM168</i>	0.93	0.92	0.96	0.99	0.86	0.81
<i>Simulated C084 GM146</i>	0.984	0.90	0.88	0.95	0.98	0.92

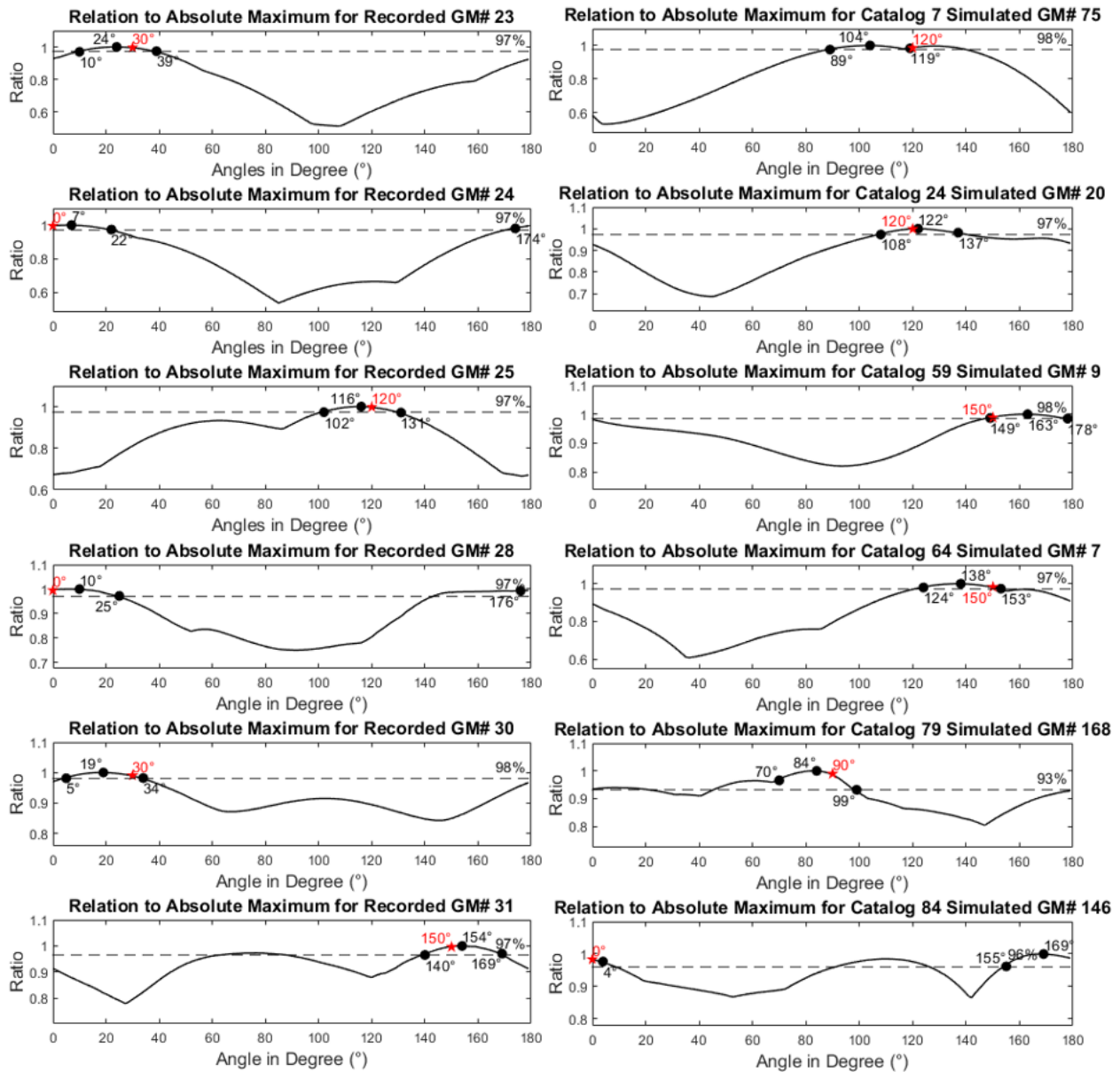


Figure 3-5: Relations of the peak Roof Drift Ratio at each 1-degree rotation (from 0° to 179°) to the absolute maximum for the MDOF model using 12 randomly selected ground motion samples. (Left 6) Recorded ground motions. (Right 6) Simulated ground motions.

3.6 Verification of OpenSees Results with Modal Analysis

This section aims to perform a sanity check on the OpenSees model. A visual comparison of the structural responses obtained by both the nonlinear time history analysis (NLTA) and the modal analysis using superposition with 10 modes in OpenSees is represented in Figure 3-6. The roof drift ratio is the structural response used for this verification. A total of 488 pairs of record ground motions excite the MDOF model at 6 selected angles. These 488 pairs of ground motions are the entire set of the earthquake records to the 288 pairs of records subset. The diagonal line represents the 1:1 ratio of the RDR between NLTHA and Modal Analysis using superposition. The maximum RDR time history using Modal Analysis (known as Response spectrum analysis using generalized coordinates) is calculated as the following equations.

$$L_{DOF,n} = \sum_{node=1}^{ALL} m_{node} \cdot \phi_{node,DOF,n} \quad M_{DOF,n} = \sum_{node=1}^{ALL} m_{node} \cdot \phi_{node,DOF,n}^2$$

Where *DOF* is either Degree-of-freedom-1 or Degree-of-freedom-3 in the horizontal plane. *n* is the *n*th mode which is up to 10 modes. *m* is the nodal mass. ϕ is the *n*th mode shape. *node* is the index of the available *node* with mass, and *ALL* is the total number of *nodes*. *L* is the scalar of seismic participation factor associated with *DOF* per *n*th mode. *M* is the scalar of generalized mass associated with *DOF* per *n*th mode.

$$\Gamma_{DOF,n} = \frac{L_{DOF,n}}{M_{DOF,n}}$$

$$U_{cnode,DOF} = \sum_{n=10}^N \Gamma_{DOF,n} \cdot \phi_{cnode,DOF,n} \cdot D_{DOF}$$

Where *D* is the 1 x (total number of acceleration history steps) spectral displacement matrix derived from the acceleration history using Central Difference Method. *Cnode* is either one of

two controlling nodes, which are the *Roof* node and the *Base* node. U is a 1 x (total number of acceleration history steps) nodal displacement matrix.

$$U_{cnode} = \sqrt{U_{cnode,DOF1} \times U_{cnode,DOF1}^T + U_{cnode,DOF3} \times U_{cnode,DOF3}^T}$$

$$RDR_{MAX} = MAX\left(\frac{U_{Roof} - U_{Base}}{H}\right)$$

Where H is the vertical distance between the *Roof* node and the *Base* node, which is the total height of the building.

In each plot, the abscissa is labeled as the maximum RDR from Modal Analysis, whereas the ordinate is marked as the maximum RDR directly collected from the OpenSee solver. The scatters of maximum RDRs in six rotational angles express broad agreement between the two results. The majority of points are concentrated below 0.005 and slightly lean toward the ordinate, and then further diverge at greater ratios. In summary, although the overall maximum RDR is not always consistent between the two results, the tendency of gathering around the diagonal line brings a perspective in which the Tcl code uses the rotating ground motion to determine whether the maximum RDR is valid.

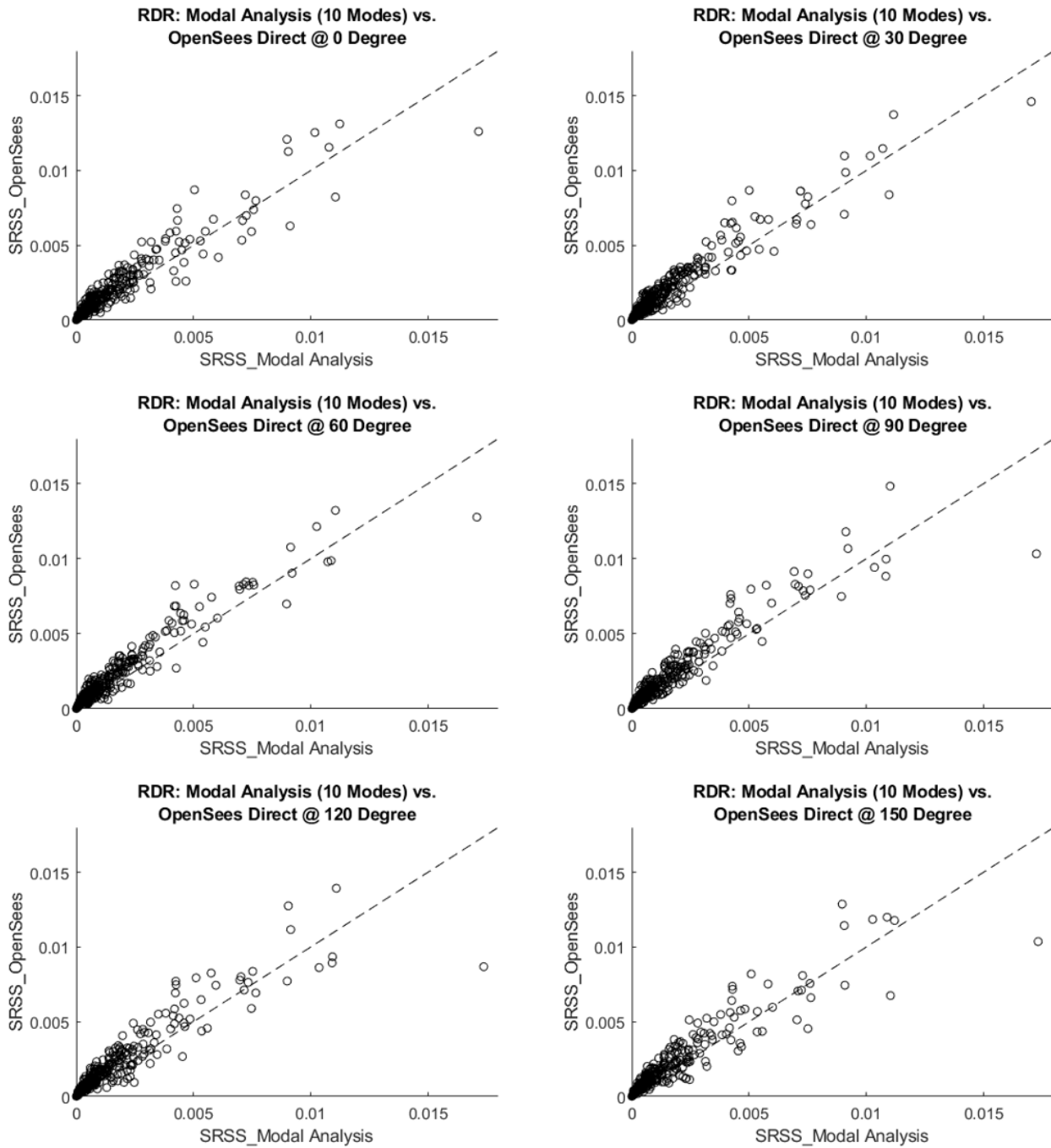


Figure 3-6: The comparison of roof drift ratios obtained from 488 recorded ground motions between Modal Analysis using superposition with 10 modes and direct records from OpenSees at six selected rotational angles.

Chapter 4 Implementation of Validation Methodology

4.1 Overview

Fayaz et al., (2020) originally suggested the validation methodology, abbreviated as MVSGM [Methodology for Validation of Simulated Ground Motions], to evaluate the similarity between the CyberShake motions and earthquake records. Rather than comparing different pairs of bi-directional ground motions, one catalogue of recorded pairs and multiple catalogues of simulated pairs that share a similar earthquake scenario is considered to see whether the recorded catalogue belongs to the population of multiple simulated catalogues combined. This paper investigates the relationships among three seismic features, including the engineering demand parameter (EDP or Rot100RDR of the tall building in this study), the event and site parameter (θ describing the earthquake scenario), and the important ground motion parameter (**RZZ** or the waveform parameter suggested by Rezaeian et al., (2015)). In each catalogue, these relationships are represented by the corresponding regression models, which define the important ground motion parameter to the engineering demand parameter (**RZZ**→EDP), the event and site parameter to the engineering demand parameter (θ →EDP), and the event and site parameter to important ground motion parameter (θ →**RZZ**). The following discussion summarizes MVSGM.

RZZ→EDP predicts the EDP as a function of seismic waveform parameters, **RZZ**. The **RZZ** parameters that influence structural responses are defined by the mathematical measure of the earthquake waveform characteristics. The **RZZ** parameter that is initially recommended to test the simulated ground motion validation includes Arias Intensity (I_A), durations (D_{0-5} , D_{0-30} , D_{5-95}), critical time reaching 45% level of I_A (t_{mid}), frequency contents (f_{mid} , f), and bandwidth parameter (ζ) for both major and minor axes, adding up to a total of 16 parameters. Among these

important ground motion parameters, only a few are sufficiently utilized in fitting the regression in this study's application. Other **RZZ** parameters are considered redundant in this high-dimensional dataset and eliminated through feature selection by filtering out the least significant parameters of **RZZ**. To further improve the regression model, dropping one or more **RZZ** parameters with a Variance Inflation Factor (VIF) Score above 10 (O'Brien, 2007) can avoid duplicates in the regression due to the effect of multicollinearity.

The feature selection uses the Boruta algorithm (Kurasu and Rudnicki, 2010), a wrapper method-based technique integrated with a random forest algorithm, to remove irrelevant and insignificant features from the entire pool of features, and to reduce the size of the **RZZ** dataset to those contributing the most to improve the accuracy of the EDP estimation for both recorded and simulated catalogues. The feature selection is performed in Python and returns the feature ranking as the horizontal bar chart in the later result. The ranking of features is designated as an integer number greater than or equal to 1. The most important **RZZ** parameter to the least important is ranked from the smallest number to the greatest number. In other words, **RZZ** parameters ranked as other than 1 are possibly being dropped. The feature selection process repeats in the recorded catalogue and each simulated catalogue independently; hence, the result of feature ranking in simulated catalogues varies. The mitigation measure can be applied by taking the mean of the sum of rankings from all simulated catalogues to attain approximate feature rankings. By using the feature selection, it results in a final set of important **RZZ** parameters. The next step is to eliminate a few more **RZZ** parameters from the finalized set that make it difficult to evaluate the relationship of each independent variable to the dependent variable in the regression model caused by the high multicollinearity. This research follows the validation methodology in which the VIF threshold of 10 is chosen. One observation on the

finalized set of **RZZ** parameters is that the same pair of major and minor **RZZ** parameters present significant collinearity, resulting in a VIF score above 10. Dropping either **RZZ** will return a small value of VIF. Moreover, the aggregate of VIF scores generated from all combined simulated catalogues is compared to the distribution of VIF scores made from the individual simulated catalogue.

Estimating the structural damage by earthquake excitation can be quantified by the EDP utilizing Nonlinear Time History Analysis. This research initially considered the following *EDPs* for tall building seismic response assessment: Roof drift ratio (*RDR*), Floor absolute acceleration (*FAA*), Floor displacement (*FD*), Inter-story drift ratio (*IDR*), Column element axial force (*CAF*), Column element deformation (*CD*), BRB element axial force (*BRBAF*), and BRB element deformation (*BRBD*). However, only the *RDR* is assessed throughout the remaining study for the consistency of the validation methodology and the tremendous amount of calculational effort needed for even one response analysis. Experimenting with other responses is encouraged for future studies. Maximum *RDR* is computed by taking the SRSS of the two horizontal responses. The absolute maximum of *RDR* is called *Rot100RDR*, which is simply achieved by rotating the bi-directional ground motions from 0° to 360° (every 30°) and then choosing the maximum. Nevertheless, the *Rot100RDR* used in this study only rotated at the selected angles discussed in the previous section to achieve about 90% of the absolute maximum as relatively acceptable criteria for the large-scale, 40-story building model with nearly five thousand nodes with six degrees of freedom.

Both second and third regression relations involve the event and site parameter as the independent variable, which is critical to quantify the effect of the earthquake nature conventionally. A seismic excitation's event and site parameter can be described using moment

magnitude, fault rupture distance, rake angle, depth to the top rupture plane, etc. As quoted in (Fayza et al., 2020), only 288 out of 488 collected recorded motions are comparable to simulated motions because the simulated motions generated from the CyberShake site are confined within 100 km of the target location with $200 \text{ m/s} < V_{s30} < 750 \text{ m/s}$. Each recorded catalogue and simulated catalogue are grouped based on this earthquake scenario to ensure similarity. The event and site parameters are advanced and converted into terms with respect to earthquake magnitude, geometric attenuation, hanging wall, shallow site response, etc., that are used in the ground motion regression model presented by Campbell and Bozorgnia (CB14). The study of this simulated ground motion validation is heavily involved in this empirical ground motion model to obtain regression coefficients such that the coefficient set from the recorded catalogue can be compared with the multiple coefficient sets from all simulated catalogues. Using box plots, we visually measure whether the recorded coefficient set falls into the desired boundary produced by the multiple simulated coefficient sets and arrive at a conclusion that the engineering demand parameter ($\theta \rightarrow EDP$) or important ground motion parameter ($\theta \rightarrow RZZs$) derived from a similar earthquake nature is statistically similar in the recorded and simulated catalogues.

Chapter 5 Results and Discussion

Fifty-one catalogues of simulated motions and one catalogue of recorded motions are utilized for this validation exercise using MVSGM. This section will discuss the results arrayed in the same sequence demonstrated in the MVSGM.

5.1 Feature Selection

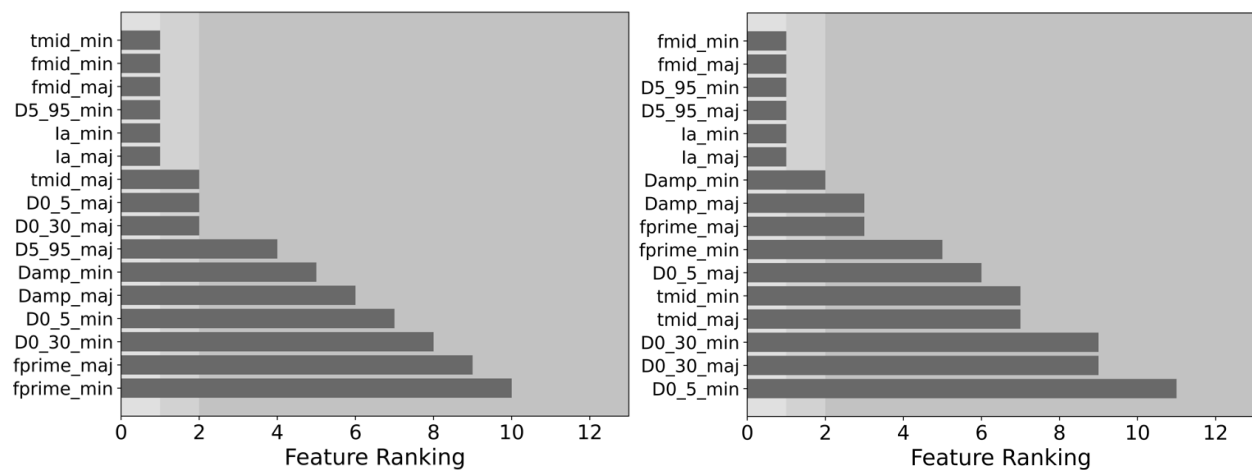


Figure 5-1: Feature ranking of all **RZZ** parameters from the recorded catalogue (left) and the 23th simulated catalogue out of 51 catalogues (right).

The important ground motion parameters, **RZZs**, describe the characteristics of the seismic waveform and are filtered by ranking the level of importance using feature selection associated with the Roof Drift Ratio of the tall building. The advantage of using feature selection is to indicate which feature is insignificant. **RZZ** parameters ranked with high numbers will be removed. Then continuing the VIF score check, **RZZ** parameters that exceeded the value of 10 are dropped to account for the effect of the multicollinearity. Eight pairs of selected **RZZ** parameters are recommended as the best parameters reflecting the intensity measure for seismic structural responses, as shown in Figure 5-1. Several features such as I_{a_major} , I_{a_minor} , f_{mid_major} ,

f_{mid_minor} , and D_{5-95_minor} are listed in rank 1 as the most significant features for the recorded catalogue in Figure 5-1 (left).

Table 5-1: The feature ranking calculated the mean of 51 simulated catalogues.

RZZ Parameter	Calculated Mean Feature Ranking
I_{a_major}	1.00
I_{a_minor}	1.00
f_{mid_major}	1.06
f_{mid_minor}	1.24
D_{5-95_major}	1.27
D_{5-95_minor}	1.41
$Damp_{major}$	2.51
f'_{major}	3.41
$Damp_{minor}$	3.43
D_{0-5_major}	3.92
t_{mid_major}	3.98
f'_{minor}	4.18
D_{0-5_minor}	4.20
t_{mid_minor}	4.47
D_{0-30_major}	4.59
D_{0-30_minor}	5.33

Those features ranked as 1 are the primary interest of this study for the evaluation of the regression relation discussed later. The remaining features are subordinated and should be abandoned. The feature ranking in the second figure represents one of 51 simulated catalogues that is noticeably consistent with how features in other simulated catalogues are ranked. The feature ranking in simulated catalogues is obtained by computing the mean of the sum of all 51 catalogues. The result shown in Table 5-1. Similarly, three pairs of **RZZ** parameters I_{a_major} , I_{a_minor} , D_{5-95_major} , D_{5-95_minor} , f_{mid_major} , and f_{mid_minor} perform well among simulated catalogues as their mean feature rankings are well below 2. Furthermore, despite D_{5-95_major} in the recorded

catalogue showing a feature ranking of 4, it is not necessary to exclude it in the important set of **RZZ** parameters since D_{5-95_major} outperforms the majority of **RZZ** parameters in each simulated catalogue. This understanding is also confirmed later, where the difference of the goodness of fit is neglectable when considering whether to include D_{5-95_major} in the regression equation. Note that the result of feature ranking for simulated catalogues is only meaningful when feature selection in the simulated catalogue is conducted independently but not combining all 51 catalogues simultaneously. Based on the observations, there are always three **RZZ** parameters (I_a , D_{5-95} , and f_{mid}), regardless of their direction, which appears to dominate the best feature ranking in both recorded and simulated catalogues.

5.2 Variance Influence Factor

The VIF score of six important **RZZ** parameters collected in feature selection is now displayed in Figure 5-2. The VIF scores of the recorded set shown in the top left figure are above 10. Similarly, in the bottom left figure, the VIF scores of the simulated set are plotted in two forms in which the solid filled black circle shows the single value of the 51 catalogues combined, while the blue line represents the range of the individual simulated catalogues (the blue circle represents the median of the range). As shown in two left figures, both the means of VIF scores computed by 51 independent simulated catalogues and the single values obtained by combined simulated catalogues or the recorded catalogue exceeding the threshold of 10 are strong indicators that multicollinearity presents in these **RZZ** parameters. Moreover, it is determined that collinearity generally occurs between the pair of the same **RZZ** parameters in these selected features. Therefore, dropping one of the components in each pair will significantly reduce the VIF score of the other component, as shown in the two figures on the right-hand side.

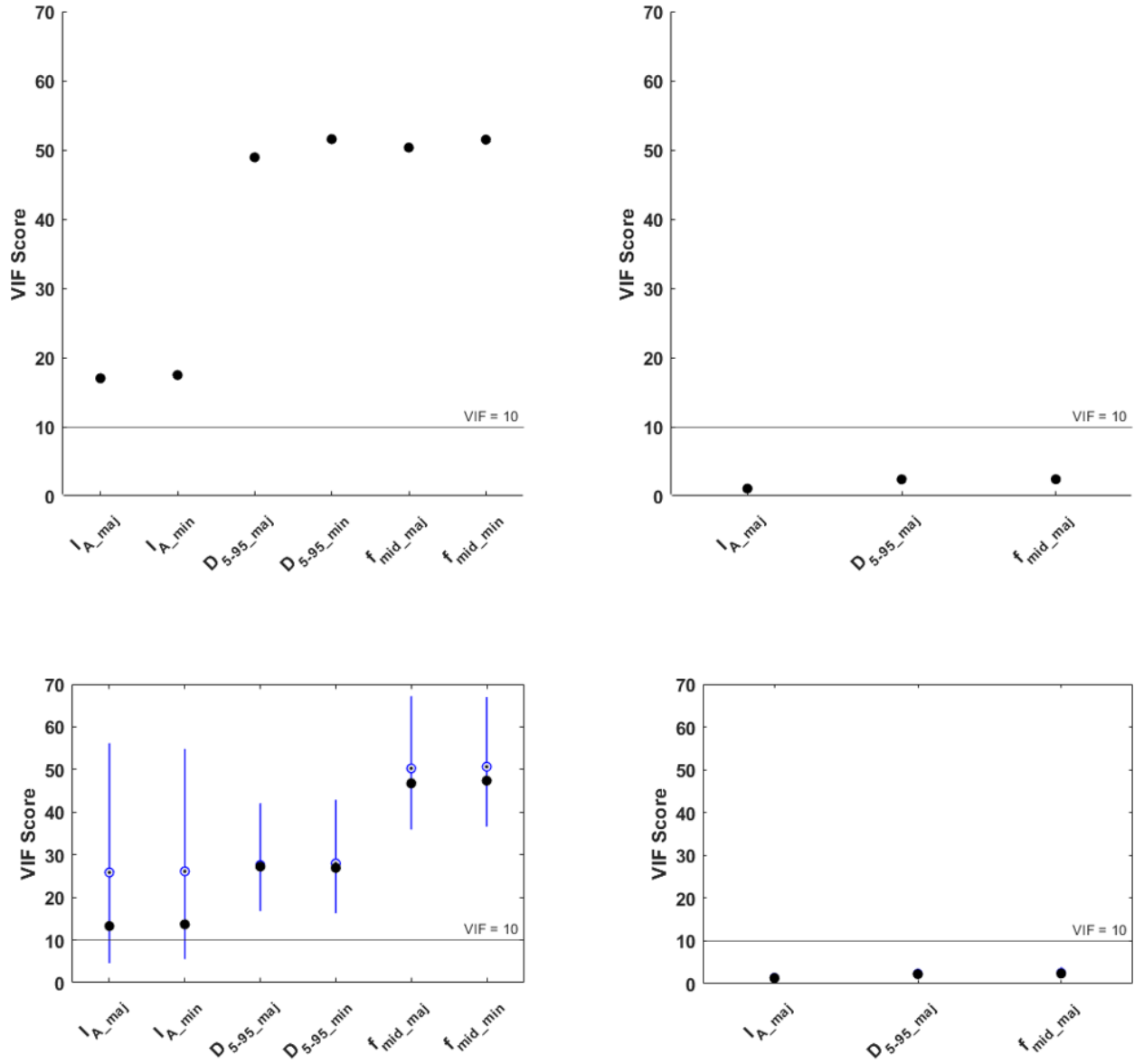


Figure 5-2: Variance Inflation Factor (VIF) scores of 6 feature selected **RZZ** parameters in the recorded catalogue (top left), the simulated catalogue (bottom left), the recorded catalogue after dropping the minor components (top right), and the simulated catalogue after dropping the minor components (bottom right).

Nevertheless, this improvement is invalid between different pairs, such that dropping either one of the components from one pair will only scantily affect the VIF scores of other pairs. Given the major component is considered the priority in this study, the minor component of each

pair is dropped from selected **RZZ** parameters. As a result, the decreasing VIF values for the major components for both the recorded catalogue and the simulated catalogues are observed in the top right and bottom right, respectively, which means the influence of collinearity is minimized. Therefore, the final set of the most important **RZZ** parameters comprises I_{a_major} , D_{5-95_major} , and f_{mid_major} for the recorded and simulated catalogues.

5.3 Regression Analysis: **RZZ** → *EDP (Roof Drift Ratio, Rot100RDR)*

The first equation uses linear regression to connect **RZZ** and *Rot100RDR*. The original regression equation from the MVSGM is adopted and modified based on the appropriate **RZZ** parameters from feature selection and VIF score. The modified version of the linear regression equation is shown in the following.

$$\ln(Rot100RDR) = b_0 + b_1 \ln(I_{a_major}) + b_2 \ln(D_{5-95_major}) + b_3 \ln(f_{mid_major}) \quad (5-1)$$

In this equation, the dependent and independent variables are obtained by transforming *EDP (Rot100RDR)* and **RZZs**, respectively in the natural logarithm form. b_1 to b_3 are the regression coefficients with b_0 as the intercept of the regression equation. The 52x4 matrix contains 1 row for the recorded catalogue and 51 rows for the simulated catalogues. Each row is individually loaded in the linear regression equation. Each row includes 1 *EDP* and 3 **RZZ** parameters to solve for the regression coefficients $b_0 - b_3$. For the simulated ground motion validation, 1 set of coefficients from the recorded catalogue is compared against 51 sets of coefficients from 51 simulated catalogues. Box plots are used to visually illustrate the locality of the coefficients from the recorded catalogue and the distribution of coefficients from the simulated catalogues.

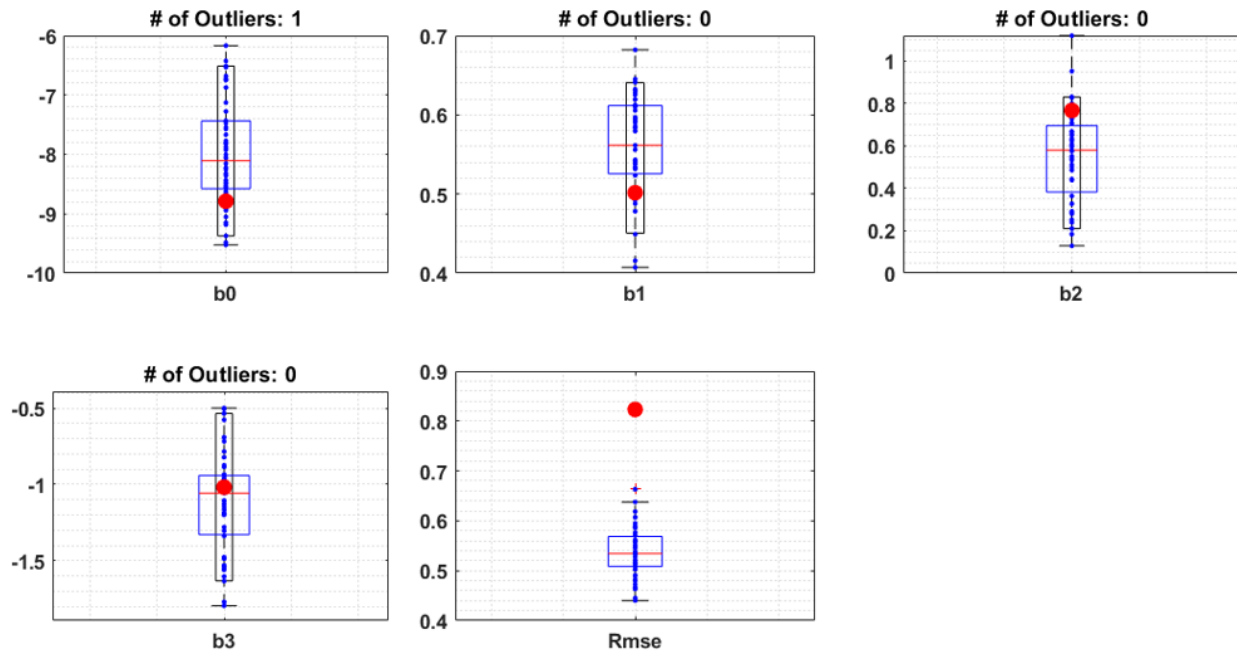


Figure 5-3: Regression intercept, coefficients, and RMSE for selected **RZZ** to Rot100RDR comparing the recorded catalogue to the simulated catalogues.

Figure 5-3 shows boxplots for regression coefficients. The coefficient for the recorded catalogue is illustrated with a red circle; the coefficient values for the simulated catalogues are shown with small blue dots. Outliers are removed from the boxplots. The wide blue rectangle box represents the typical interquartile range of the middle 50% of the simulated coefficients that is enclosed between the lower quartile (the lower 25th percentile) and the upper quartile (the upper 75th percentile), with the median (the 50th percentile) red mark dividing the blue box into two equal percentage. In addition to the classic blue box, the 90% confidence interval (specified as the Preferred Percentile Range) of the simulated coefficient in the population, defined by the narrow black rectangle box, is added to the boxplot such that the recorded coefficient falls between the 5th to 95th percentile boundaries is considered acceptable with regard to the statistical similarity utilizing the **RZZ**→EDP regression analysis. Two extremes, the minimum (the 0th percentile) and the maximum (the 100th percentile), are shown as the horizontal bar at the end of both the

lower and upper whiskers, representing outside the interquartile range in the dashed line. Results are shown for b_0 , b_1 , b_2 , and b_3 , respectively. The last figure for Root Mean Square Error (RMSE) is irrelevant to the similarity comparison between the recorded catalogue and simulated catalogues but rather to reveal how concentrated the *Rot100RDR* given the selected **RZZ** parameters is around the regression line. The lower RMSE for the simulated catalogues indicates that the important ground motion parameters (independent variables) in the recorded catalogue are more diverse.

The Adjusted R-Squared (R_{adj}^2) shows the goodness of fit. $R_{adj}^2 = 0.59$ for the recorded catalogue is considered a moderate score. The overall goodness of line fit in simulated catalogues perform better than the recorded catalogue, as the R_{adj}^2 for simulated catalogues varying between 0.56 and 0.85 gives the mean of 0.75 and the median of 0.76, which both scores (≥ 0.7) are generally acceptable such that the selected **RZZ** parameters highly correlate with *Rot100RDR*. Given that **RZZ** parameters, namely I_{a_major} , D_{5-95_major} , and f_{mid_major} , are best capable of predicting the *Rot100RDR* in feature selection, the trends of regression functions between the recorded catalogue and simulated catalogues are similar. This renders both the intercept and corresponding regression coefficients for the recorded catalogue successfully lying inside the distribution of data points for the simulated catalogues in Figure 5-3. Besides the recorded coefficient (b_3) for f_{mid_major} , which falls to the typical interquartile range, other plots such as b_0 for the intercept, b_1 for I_{a_major} , and b_2 for D_{5-95_major} merely stay in the 90% preferred percentile range, in which any coefficient associated with the recorded catalogue appears as the part of the variance in the simulated catalogues. The **RZZ** parameters are efficient and sufficient to predict *EDP* to some extent. Therefore, the use of simulated ground motion can produce

results potentially similar to the recorded ground motion, as presented that the regression coefficient obtained by the recorded catalogue is considered a subset of the simulated catalogues.

5.4 Regression Analysis: $\theta \rightarrow EDP$ (*Roof Drift Ratio, Rot100RDR*)

To investigate the statistical similarity between the recorded catalogue and simulated catalogues, the independent variables in the regression equation for $\theta \rightarrow EDP$ use the functional terms (f -terms) that are transformed by the combination of the event and site parameters (θ s) for EDP estimation. In the nonlinear regression analysis, the formation of the natural logarithm of EDP is not proportionally contributed by the individual θ but rather the mixed effect of functional terms used in the Ground Motion Model developed by Campbell and Bozorgnia (2014). In Equation 5-2, the regression equation used for the application in this study is determined to be unchanged from the MVSGM where the equation is originally modified from

$$\ln(Rot100RDR) = c_0 + c_1 M_w + (c_5 + c_6 M_w) \ln(\sqrt{R_{RUP}^2 + c_7^2}) + c_8 F_{RV} + c_{10} f_{hng} + c_{11} f_{site,G1} + f_{site,G2} + c_{14} f_{sed,1} + c_{16} f_{sed,2} + c_{18} f_{hyp} \quad (5-2)$$

CB14; however, certain coefficients (e.g., k_i , a_i , and h_i) associated with the CB14 model other than the unsolved $c_0 - c_{20}$, are structural model period dependent and not shown in the equation. Hence these particular coefficients will be altered to values specified for the longer period of the tall building when compared to those coefficients used for the bridge in the MVSGM. The regression equation shown above has already been optimized by shortening and removing unnecessary terms that are not applicable, thereby the presented inputs of the independent variables (θ and f -term) characterize the scaling of ground motions with regard to magnitude term (f_{mag}), geometric attenuation term (f_{dis}), style of faulting term (f_{flt}), hanging wall term (f_{hng}),

shallow site response term (f_{site}), basin response term (f_{sed}), and hypocentral depth term (f_{hyp}) defined in CB14. The information on how these f -terms are derived from θ values and Equation 5-2 is formed can be found in Fayaz et al. (2020). A summary of the breakdown of which regression coefficient is related to which f -term is listed in Table 5-2 below.

Table 5-2: Summary of CB14 functional terms with the corresponding regression coefficients

Functional Term	CB14 f -term	Corresponding Coefficient
Earthquake Magnitude	f_{mag}	c_0, c_1
Geometric Attenuation	f_{dis}	c_5, c_6, c_7
Style of Faulting	f_{flt}	c_8
Hanging Wall	f_{hng}	c_{10}
Shallow Site Response	f_{site}	c_{11}
Basin Response	f_{sed}	c_{14}, c_{16}
Hypocentral Depth	f_{hyp}	c_{18}

The validation of simulated ground motion continues to utilize the box plot with whiskers shown in Figure 5-4 to evaluate the similarity of the regression coefficients for the $\theta \rightarrow EDP$ between the recorded catalogue and simulated catalogues. The wide spread of RMSEs for simulated catalogues shows that the variation in f -term describing Rot100RDR varies with catalogue, and the RMSE for the recorded catalogue is within the upper portion of this spread. The overall RMSEs of the tall building model for both the simulated catalogue and the recorded catalogue are double or nearly triple the bridge model in the MVSGM. The dynamic response of high-rise buildings may explain the great difference in RMSEs associated with the *Rot100RDR*. We postulate it is due to the long period and cumulative column shortening over the height of the tall building. Although, as stated in the statistical literature from other authors, the unsolved regression coefficient c_7 inside the square root bracket that is interacted with c_5 and c_6 leads to

nonlinear regression and influences both the R^2 and R_{adj}^2 , which makes it difficult to measure the goodness of fit of the model appropriately. Thus, R_{adj}^2 is used with caution to assess the fit of the nonlinear regression model. The R_{adj}^2 for the recorded catalogue is 0.73. For the simulated catalogues, the mean of 0.70 and the median of 0.70 computed in the range fluctuating from 0.27 to 0.88 are observed. To a large extent, R_{adj}^2 values above 0.7 for the recorded and the mean and median of simulated are considered acceptable quantities for the $\theta \rightarrow EDP$.

In addition to Figure 5-4, c_0 , c_1 , c_5 , c_6 , c_7 , c_8 , c_{10} , c_{16} , and c_{18} for the recorded catalogue shown in red circles are inside the 90% preferred percentile range of simulated catalogues; c_1 , c_7 , and c_{10} of which fall to the typical interquartile ranges. This finding generally matches what was suggested in Fayaz et al. (2020); both c_{11} (shallow site response) and c_{14} (basin response) of the recorded coefficients are far from the spreads of simulated coefficients. This finding shows that the structure type may not cause such discrepancies between the recorded and simulated ground motions. Notwithstanding, the overall distribution of simulated coefficients comprises the trend of the recorded coefficient based on the 90% preferred percentile range.

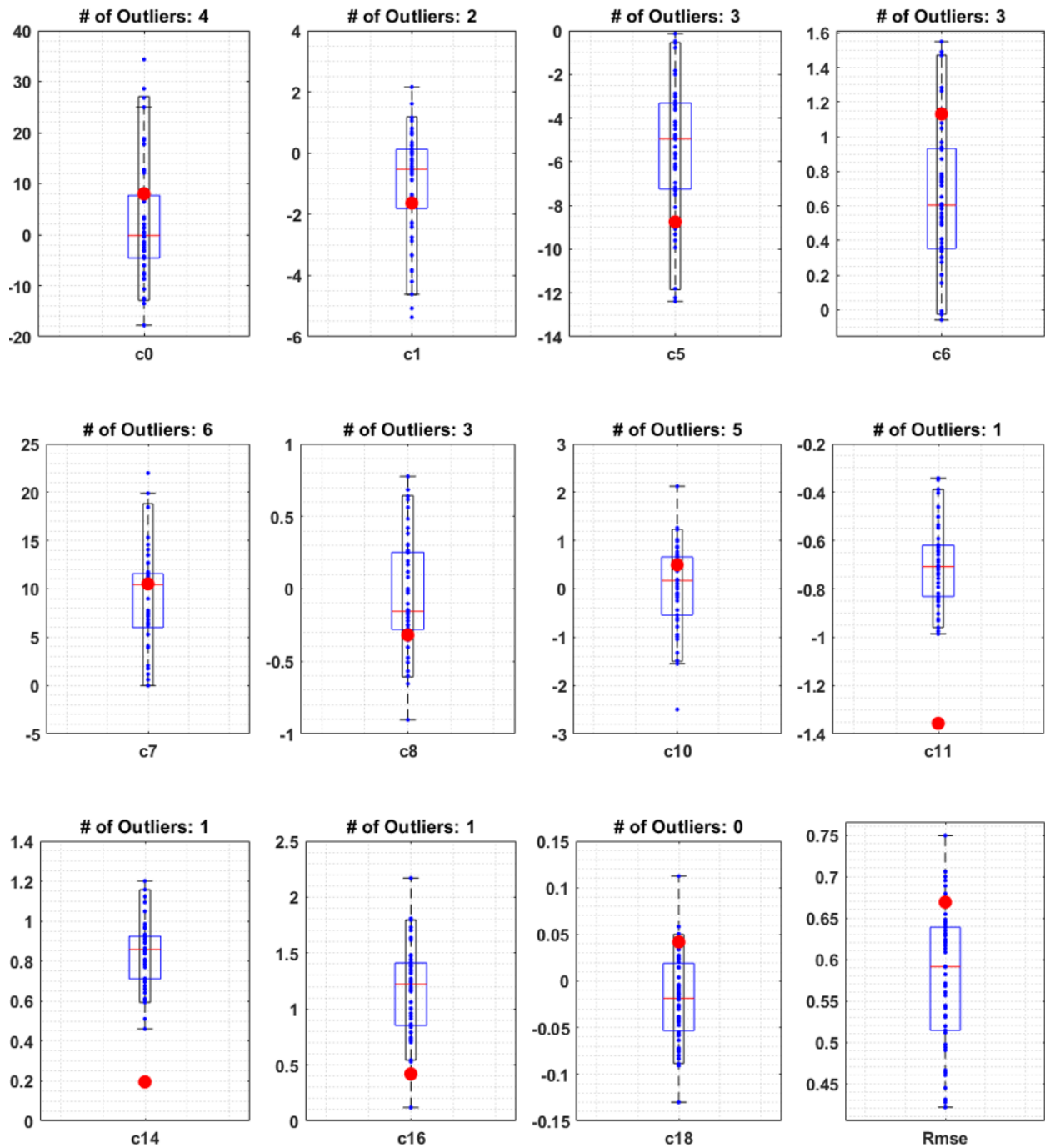


Figure 5-4: Regression intercept, coefficients, and RMSE for θ to Rot100RDR comparing the recorded catalogue to the simulated catalogues.

5.5 Regression Analysis: $\theta \rightarrow RZZ$ (I_{a_major})

As previously discussed, relations of both the $\theta \rightarrow EDP$ and $RZZ \rightarrow EDP$ have shown that the simulated ground motion is similar to the recorded ground motion and produces a comparable structural response. Therefore, continuing to verify whether simulated ground motion can substitute the recorded ground motion for the engineering application, the last part of the three-way relationship, the $\theta \rightarrow RZZ$, is conducted to backcheck each independent variable (the selected RZZ parameters) in Equation 5-1. This discussion will first validate the regression relation of the event and site parameters to Arias Intensity. The regression equation for the $\theta \rightarrow I_a$ is the same equation for the $\theta \rightarrow EDP$ with minor modification.

$$\ln(I_{a_major}) = c_0 + c_1 M_w + (c_5 + 0.416 M_w) \ln(\sqrt{R_{RUP}^2 + 4.869^2}) + c_8 F_{RV} + c_{10} f_{hng} + c_{11} f_{site,G1} + f_{site,G2} + c_{14} f_{sed,1} + c_{16} f_{sed,2} + c_{18} f_{hyp} \quad (5-3)$$

Equation 5-3 shows the relationship between the f -terms and I_a . The geometric attenuation term is altered so that c_6 and c_7 are assigned to constant values of 0.416 and 4.869, respectively. These two constant values are reported as the goodness-of-fit of the regression coefficients for Arias Intensity in Campbell and Bozorginia (2019). Several researchers (Abrahamson et al., 2016; Bahrapouri et al., 2020; Fayaz et al., 2020) have pointed out that the two coefficients (c_6 and c_7 in Equation 5-2) are generally related to the magnitude and distance term and are highly correlated to each other while estimating I_a . Forcing coefficients c_6 and c_7 fixed in the geometric attenuation term allows for minimizing errors when determining other coefficients; thereby, Equation 5-3 is being a linear regression form.

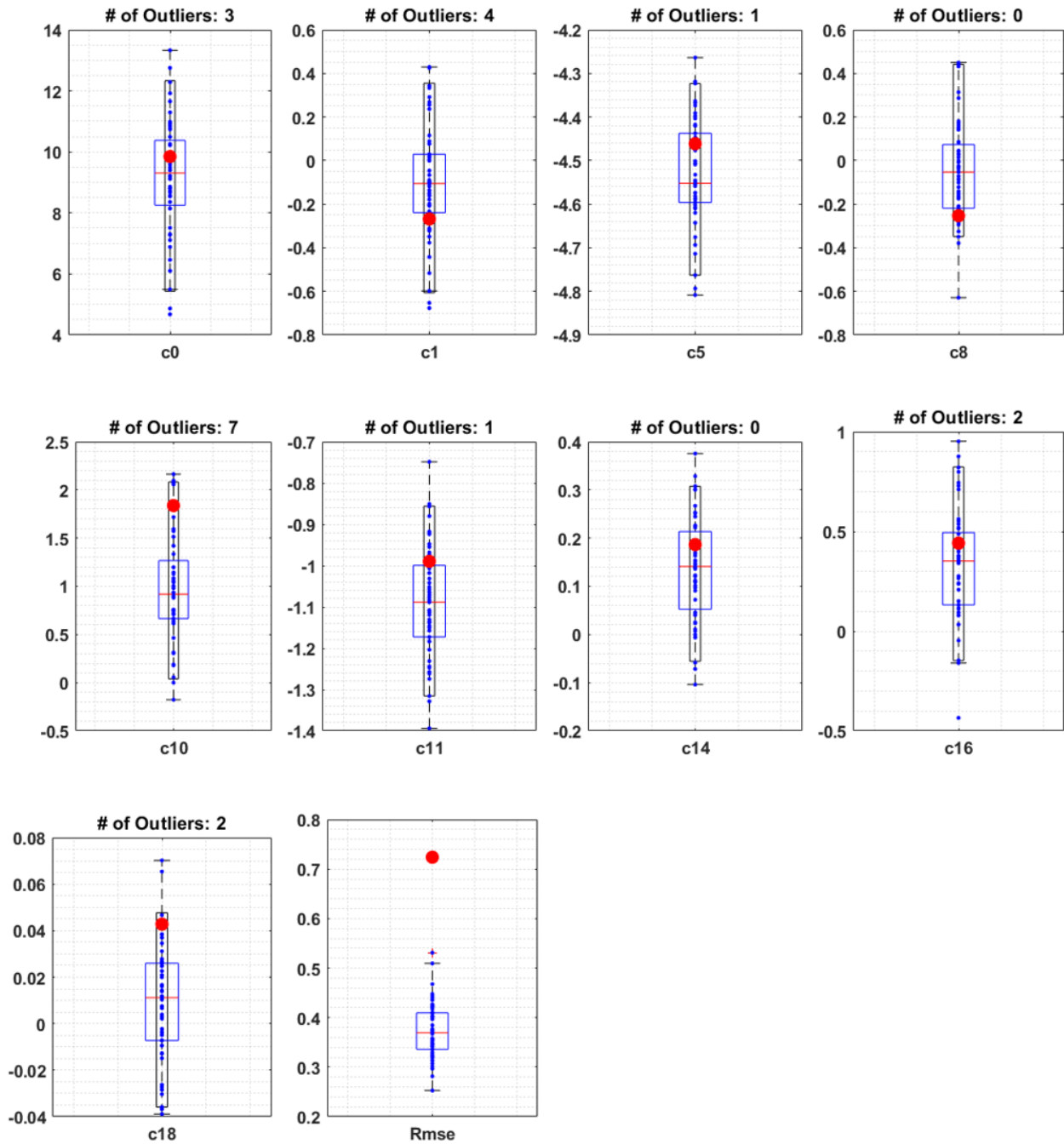


Figure 5-5: Regression intercept, coefficients, and RMSE for θ to I_{a_major} comparing the recorded catalogue to the simulated catalogues.

The result of fitting the linear regression θ to I_{a_major} for the recorded catalogue and the simulated catalogues are shown in Figure 5-5. The $R_{adj}^2 = 0.75$ is lower than the mean and

median of R_{adj}^2 for simulated catalogues (0.91 and 0.92, respectively), with a range of 0.80 to 0.96. The R_{adj}^2 of the linear regression for θ to EDP expresses how efficiently the linear model can fit the site and event parameters θ . The comparison of the regression coefficient between the recorded catalogue and simulated catalogues in Figure 5-5 shows all coefficients such as c_0 , c_1 , c_5 , c_8 , c_{10} , c_{11} , c_{14} , c_{16} , and c_{18} stay inside the 90% preferred percentile range, particularly, c_0 , c_5 , c_{14} , and c_{16} which fall to the typical interquartile range. This result demonstrates that the simulated catalogues can capture the trend of linear regression θ to I_{a_major} for the recorded catalogue. The RMSE for the recorded catalogue is approximate twice the mean of 51 simulated catalogues, which shows the residual in the I_{a_major} estimation given the f -terms for the recorded set is still greater than the simulated set. The difference in RMSE conforms to the result for the bridge model in the MVSGM. This outcome is consistent with other regression models regarding the $\mathbf{RZZ} \rightarrow EDP$ and the $\theta \rightarrow EDP$. To summarize, the regression models for $\mathbf{RZZ} \rightarrow EDP$, $\theta \rightarrow EDP$, and $\theta \rightarrow \mathbf{RZZ}$ have larger R_{adj}^2 for simulated sets than the recorded set. Therefore, the simulated ground motion generated by the CyberShake 15.12 simulation may be short of the variation regarding the ground motion parameters (θ).

5.6 Regression Analysis: $\theta \rightarrow \mathbf{RZZ}$ (D_{5-95_major})

The fitting regression equation for the $\theta \rightarrow D_{5-95_major}$ that validates the simulated ground motions for the tall building is acquired from the MVSGM and shown in Equation 5-4. It is a predictive model proposed by (Dabaghi and Kiureghian, 2014). The important \mathbf{RZZ} parameter, D_{5-95_major} , is purposely selected to maintain the consistency in the major axis of the intensity

$$\ln(D_{5-95_major}) = \beta_0 + \beta_1 M_w + \beta_3 F_{RV} f_{flt,Z} + \beta_4 \ln(\sqrt{R_{RUP}^2 + 6^2}) + \beta_6 \ln(V_{s30}) \quad (5-4)$$

measure (e.g., I_{a_major} , D_{5-95_major} , and f_{mid_major}) for the validation methodology applied to a tall building model in this study. Because Equation 5-4 looks similar to the Cambell and Bozorgnia (2008) GMPE, it is reasonable to believe that this regression model incorporates the effects of earthquake magnitude, distance, style-of-faulting, and shallow site response. Figure 5-6 shows the RMSE for the recorded catalogue is less than the 25th percent of the simulated catalogues, which implies the inputs of the aforementioned functional terms for the simulated catalogues are sufficient to produce the variation in D_{5-95_major} . The recorded catalogue has $R_{adj}^2 = 0.55$, which is close to 0.5, and the simulated catalogues only have the mean of $R_{adj}^2 = 0.49$ and the median of $R_{adj}^2 = 0.50$ from a range of 0.23 to 0.78. The R_{adj}^2 for the recorded catalogue is acceptable; however, R_{adj}^2 for simulated catalogues with a mean less than 0.5 suggests a weak linear relationship between D_{5-95_major} and θ . Although the figures show that the trend of recorded regression is similar to the simulated regressions as all recorded coefficients fall to the distributions of the simulated coefficients, Equation 5-4 underperforms and may not be a good predictive model for describing the duration from 5 to 95% of Arias Intensity due to the low R_{adj}^2 values.

Furthermore, it is seen in Figure 5-1 that D_{5-95_minor} has a better feature ranking compared to D_{5-95_major} for the recorded catalogue; inversely, the D_{5-95_major} for simulated catalogues is generally ranked a little better than D_{5-95_minor} . For comparison, an additional regression study for D_{5-95_minor} is conducted to see the goodness of fit using the suggested Equations 5-1 and 5-4. The recorded R_{adj}^2 and the simulated mean of R_{adj}^2 and median of R_{adj}^2 for D_{5-95_minor} are observed as 0.52, 0.49, and 0.49, respectively. Additionally, the difference in RMSEs between D_{5-95_major} is neglectable. In general, the value of R_{adj}^2 below 0.70 means the predictive power regarding the

regression equation is neither unacceptable nor desirable; however, it should be abandoned if below 0.5.

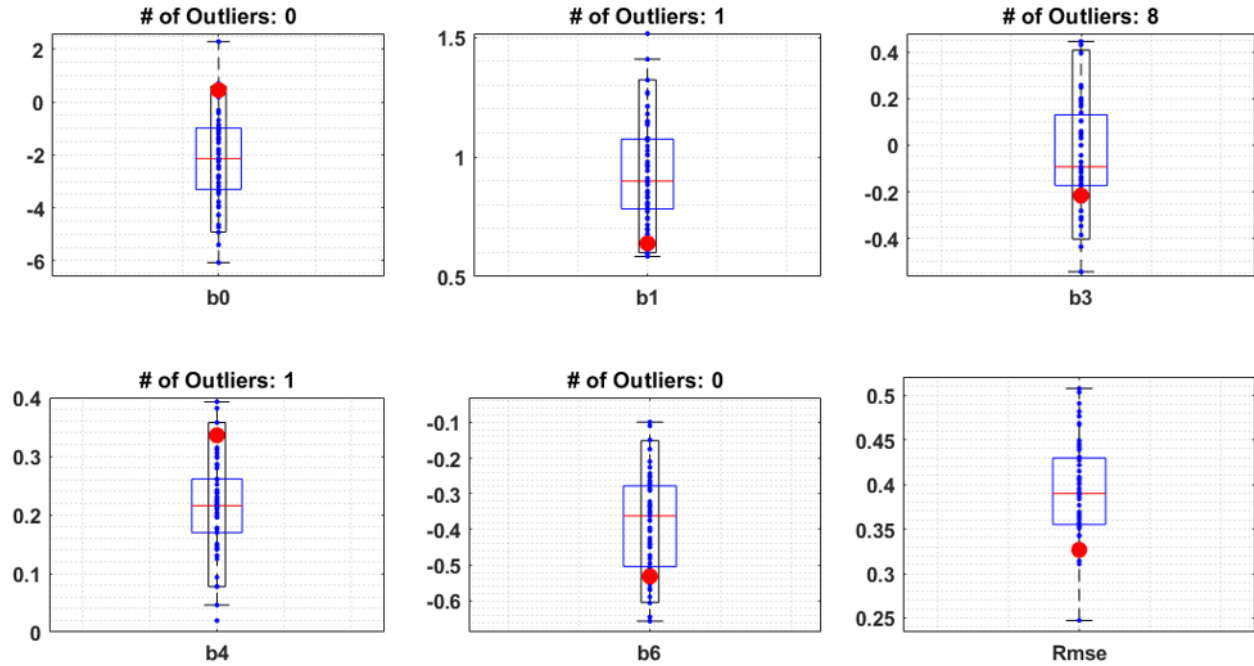


Figure 5-6: Regression intercept, coefficients, and RMSE for θ to D_{5-95_major} comparing the recorded catalogue to the simulated catalogues.

5.7 Regression Analysis: $\theta \rightarrow RZZ (f_{mid_major})$

The comparison of the regression coefficients for the $\theta \rightarrow f_{mid_major}$ between the recorded catalogue and simulated catalogues employed the equation from the MVSGM, as shown in Equation 5-5. This equation is another regression model suggested by (Dabagni & Kiureghian, 2018) to predict the frequency content using the simulated ground motions. The results of the coefficients are shown in Figure 5-7. The values of R_{adj}^2 obtained for the recorded catalogue, and the mean and median of simulated catalogues (measured in a range from 0.06 to 0.5) are 0.294, 0.22, and 0.20, respectively. Equation 5-5 may misrepresent the best-fit line of the θ to f_{mid_major} ,

as the regression model poorly captures the variance trend in the dependent variable (f_{mid_major}). Although Figure 5-7 shows coefficients β_0 and β_1 for the recorded catalogue fall to the interquartile range and the 90% preferred percentile range, except for β_6 , the low R_{adj}^2 values make the comparison between the recorded and simulated catalogues meaningless. A follow-up frequency content study on the regression equation is recommended; it may require introducing new function terms and even other independent variables (θ) to complete the integrality of the regression model for the best predictive power possible for θ to f_{mid_major} .

$$\ln(f_{mid_major}) = \beta_0 + \beta_1 M_w + \beta_6 \ln(V_{s30}) \quad (5-5)$$

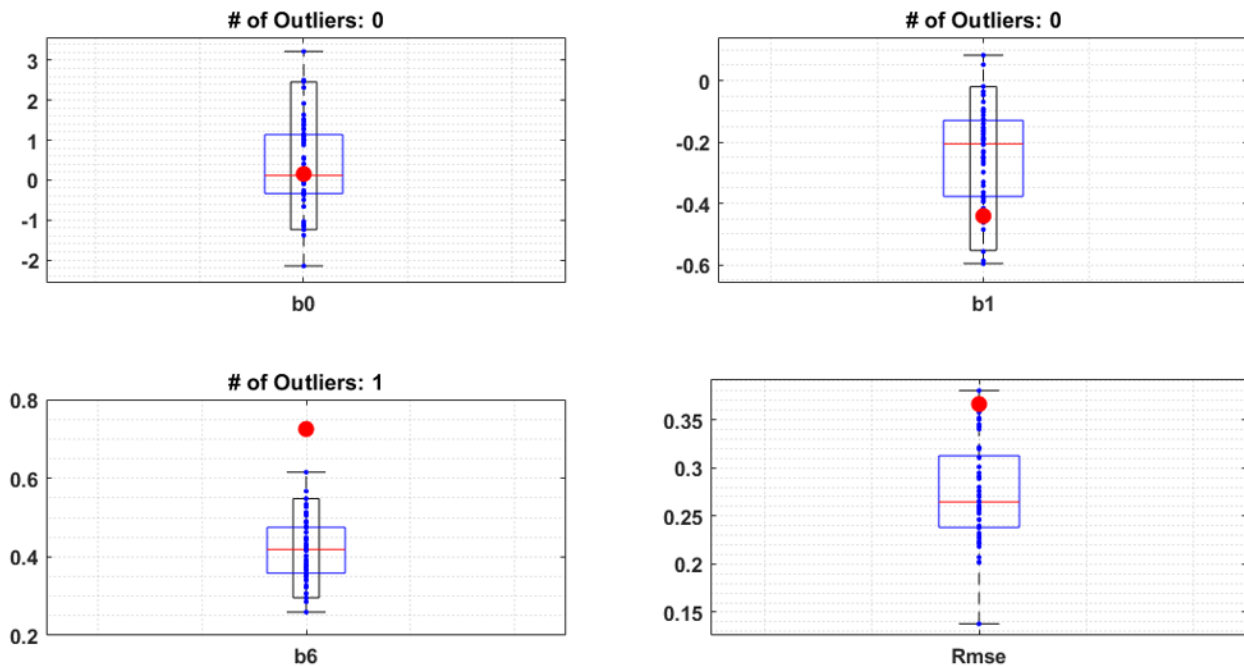


Figure 5-7: Regression intercept, coefficients, and RMSE for θ to f_{mid_major} comparing the recorded catalogue to the simulated catalogues.

5.8 Additional Simulated Ground Motion Validation Result

This section includes the results using the validation methodology developed by (Munjy et al., 2021). The latter test a null hypothesis that the recorded and simulated regression coefficients are similar by performing an analysis of Variance (ANOVA) on the nested model, which combines both recorded and simulated regression models used as the base regression model for both the recorded and simulated catalogues. Each simulated regression is combined with the same recorded regression. As a result, 51 results of ANOVA are presented in Table 5-3. The significance level of 0.05 is chosen to test the null hypothesis. All p-values are well below the selected significance level. The result indicates all nested models reject the null hypothesis that the recorded and simulated regression coefficients (b_0 , b_1 , b_2 , and b_3) are equal to each other, and the simulated model is considerably dissimilar to the recorded model. The detailed procedures of how the nested model is built can be found in the author's paper and this paper will only present the final result of ANOVA.

Figure 5-8 shows the trendlines of the independent variable in Equation 5-1 to see how **RZZ** parameters will affect the target EDP (Rot100RDR). In each plot, there are 51 simulated catalogue trendlines in red and 1 recorded catalogue trendline in black. The simulated and recorded regression share a similar slope for Arias Intensity, except the intercept does not tend to line up. The duration and frequency content do not predict the EDP well, as the slopes of red and black lines are significantly different. This result is consistent with earlier findings herein that Arias Intensity tends to have the highest predicting power for building seismic responses.

Table 5-3: *p*-value from ANOVA Using Combined Recorded and Simulated Catalogue Regression Models

GM Catalogue	<i>p</i> -value	GM Catalogue	<i>p</i> -value	GM Catalogue	<i>p</i> -value
Rec+Sim1	8.55E-102	Rec+Sim21	1.20E-126	Rec+Sim41	3.90E-193
Rec+Sim2	1.03E-134	Rec+Sim22	1.71E-88	Rec+Sim42	1.18E-107
Rec+Sim3	9.83E-119	Rec+Sim23	1.38E-197	Rec+Sim43	1.41E-124
Rec+Sim4	2.61E-138	Rec+Sim24	1.23E-141	Rec+Sim44	9.38E-150
Rec+Sim5	2.69E-138	Rec+Sim25	1.85E-114	Rec+Sim45	1.18E-150
Rec+Sim6	1.50E-131	Rec+Sim26	9.93E-171	Rec+Sim46	7.91E-142
Rec+Sim7	5.55E-124	Rec+Sim27	1.52E-207	Rec+Sim47	2.19E-143
Rec+Sim8	1.17E-118	Rec+Sim28	6.54E-110	Rec+Sim48	3.24E-125
Rec+Sim9	8.94E-140	Rec+Sim29	1.17E-148	Rec+Sim49	2.98E-138
Rec+Sim10	3.79E-137	Rec+Sim30	7.93E-205	Rec+Sim50	1.72E-96
Rec+Sim11	1.04E-188	Rec+Sim31	4.92E-128		
Rec+Sim12	1.29E-136	Rec+Sim32	1.41E-204		
Rec+Sim13	1.18E-171	Rec+Sim33	4.28E-99		
Rec+Sim14	1.21E-107	Rec+Sim34	1.02E-145		
Rec+Sim15	1.37E-132	Rec+Sim35	2.38E-102		
Rec+Sim16	1.56E-140	Rec+Sim36	1.24E-156		
Rec+Sim17	4.20E-140	Rec+Sim37	7.53E-144		
Rec+Sim18	1.21E-162	Rec+Sim38	2.87E-151		
Rec+Sim19	1.07E-200	Rec+Sim39	8.89E-190		
Rec+Sim20	5.93E-147	Rec+Sim40	5.93E-109		
				Maximum	1.71E-88
				Minimum	1.52E-207

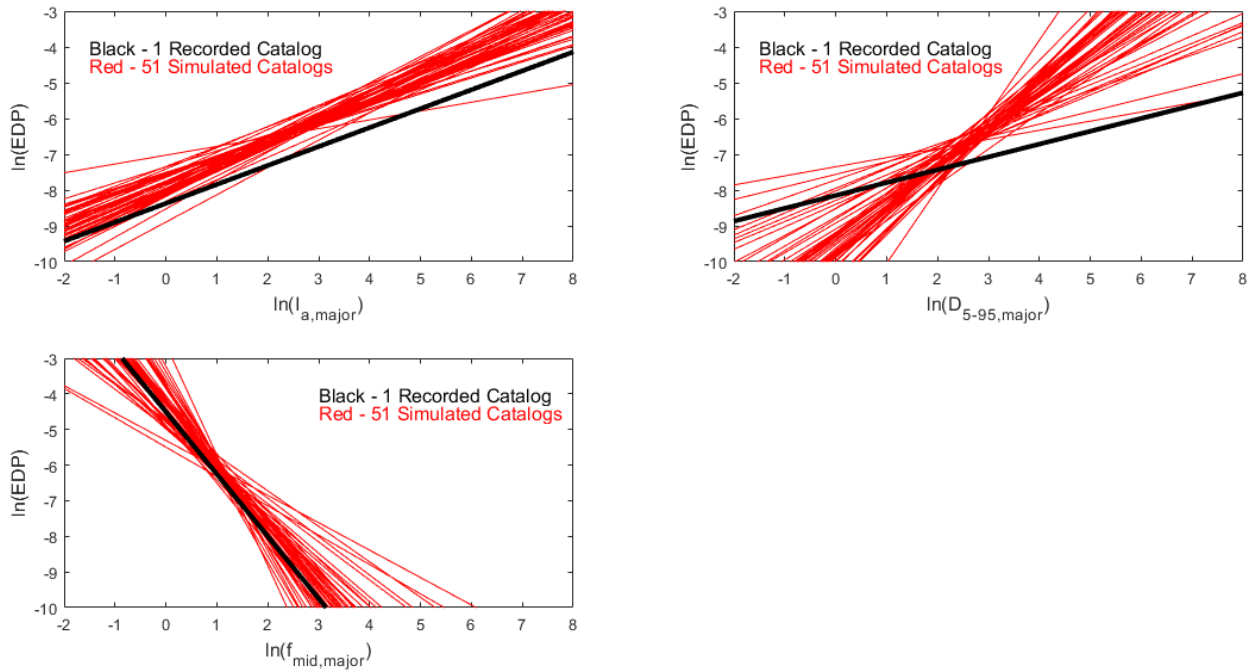


Figure 5-8: The trendlines of **RZZ** Parameter and EDP (Roof Drift Ratio) Comparing the Recorded Catalogue and 51 Individual Simulated Catalogues

Chapter 6 Summary and Conclusions

6.1 Summary

Comprehensive research following Fayaz et al. (2020) methodology for validating simulated ground motion is executed for a seismic response assessment of a tall building structure. Although the results are not entirely satisfying, they shed light on the similarity of simulated and recorded ground motions for tall buildings' structural response assessment. One catalogue of 288 pairs of recorded ground motions from NGA-West2 and 51 catalogues of simulated ground motions with a total of 14,005 pairs of CyberShake (15.12) motions are utilized to compare the statistical similarity of three relationships: $\mathbf{RZZ} \rightarrow \mathbf{EDP}$, $\boldsymbol{\theta} \rightarrow \mathbf{EDP}$, and $\boldsymbol{\theta} \rightarrow \mathbf{RZZ}$.

The earthquake event and site parameters, $\boldsymbol{\theta}$, describe the earthquake's nature, including the earthquake moment magnitude, the rupture distance, and the shear wave velocity in the top 30 meters. The estimation of the intensity measure and EDP use Ground Motion Prediction Equations suggested by several authors, namely Fayza et al. (2020), Campbell & Bozaorgnia (2014) and (2019), and Dabaghi & Kiureghian (2018), with modifications that better suit the tall building model in this paper. The engineering demand parameter, EDP, is obtained by running a nonlinear time history analysis on the MDOF model of a 40-story tall building. The primary interest of response assessment is the maximum roof drift ratio that occurred at the critical ground motion intercept angle. Thus, ground motion rotations with six selected angles, 30°, 60°, 90°, 120°, and 150°, are applied to the MDOF model to determine the relative maximum RDR, denoted as Rot100RDR.

Three \mathbf{RZZ} parameters, I_{a_major} , D_{5-95_major} , and f_{mid_major} are shortlisted from the original 16 \mathbf{RZZ} parameters that were selected by (Rezaeian et al., 2015) to represent important

waveform characteristics such as Arias Intensity, significant duration, frequency content, damping, for pairs of orthogonal and horizontal ground motions. Feature selection and the collinearity check with VIF scores are used to determine the most relevant set of **RZZ** parameters from all 16 **RZZ** parameters that are possibly correlated. **RZZ** parameters with the worst rankings and high VIF scores are eliminated to improve the accuracy of estimating EDP for the MDOF model. The regression analysis results show that I_{a_major} , D_{5-95_major} , and f_{mid_major} are sufficient and efficient enough to predict the structural response in the validation methodology for simulated ground motions.

6.2 Conclusions

The following paragraphs enumerate the major findings of this study:

1. The critical angle resulting from the maximum value of Arias Intensity does not necessarily indicate the maximum structural response obtained from all rotated angles for an MDOF model. Maximum Roof Drift Ratio does not necessarily happen at the same orientation where a maximum Arias intensity is achieved.
2. The limitation of using a simplified 2DOF model to estimate the critical angle for the maximum response of the MDOF model is identified. It is shown that the polarization of peak responses for the MDOF and 2DOF models does not align. The biggest difference in critical angles between the two models can be at most 60°. The simplified 2DOF model may not be suitable for finding the critical angle for a structural model's maximum response with a long fundamental period.
3. With the intensive computational cost to obtain the maximum response at the critical angle for the MDOF model, an efficient solution is proposed: selecting six rotational

angles (i.e., 0, 30, 60, 90, 120, and 150 degrees) to achieve about 90% of the absolute maximum of RDR. This approach significantly reduces the computational effort and can attain an acceptable value without repeating a series of ground motion rotations from 0° to 180° with a 1° increment.

4. For all linear regression models, the overall RMSE for the recorded catalogue is higher than that for the simulated catalogues, which explains why the ground motion generated from CyberShake (15.12) is less diverse than the recorded ground motion.
5. Results show that the response of the tall building used in this study to simulated ground motion follows the same trend of recorded ground motions. Regression describing the relationship of $\mathbf{RZZ} \rightarrow EDP$, $\theta \rightarrow EDP$, and $\theta \rightarrow \mathbf{RZZ}$ for the recorded catalogue fall into the Preferred Percentile Range ($5^{\text{th}}\% \leq c_{\text{simulated}} \leq 95^{\text{th}}\%$) or even the Typical Interquartile Range ($25^{\text{th}}\% \leq c_{\text{simulated}} \leq 50^{\text{th}}\%$) formed by simulated coefficients. For the simulated catalogues, $\mathbf{RZZ} \rightarrow Rot100RDR$, $\theta \rightarrow Rot100RDR$, and $\theta \rightarrow I_{a_major}$ show both the important waveform parameters and the event and site parameters appropriately predict the variance in the engineering structural response and \mathbf{RZZ} parameters with the use of corresponding GMPEs. The CB14 equation poses the highest predicting power in both the recorded catalogue and the simulated catalogue as both adjusted R-squares are the highest for the relationships of $\theta \rightarrow Rot100RDR$ and $\theta \rightarrow I_{a_major}$. The frequency content parameter shows the weak similarity of $\theta \rightarrow f_{mid_major}$ between the recorded and simulated catalogues with low adjusted R-squares values. Additionally, $\theta \rightarrow Rot100RDR$ shows that the recorded catalogue and the simulated catalogues do not share similar site information such as shallow site response and basin response.

Reference

- Abrahamson, C., Shi, H.-J. M., & Yang, B. (2016). Ground-Motion Prediction Equations for Arias Intensity Consistent with the NGA-West2 Ground-Motion Models. *Pacific Earthquake Engineering Research Center*. PEER Report No. 2016/05
- Abrahamson, C., Shi, H.M., Yang, B. Ground-Motion Prediction Equations for Arias Intensity Consistent with the NGA-West2 Ground-Motion Models. *Pacific Earthquake Engineering Research Center*. PEER Report No. 2016/05
- Akkar, S., & Bommer, J. J. (2010). Empirical Equations for the Prediction of PGA, PGV, and Spectral Accelerations in Europe, the Mediterranean Region, and the Middle East. *Seismological Research Letters*, 81(2), 195–206. <https://doi.org/10.1785/gssrl.81.2.195>
- Amin, M., & Ang, A. H. S. (1968). Nonstationary Stochastic Models of Earthquake Motions. *Journal of the Engineering Mechanics Division*, 94(2), 559–584. <https://doi.org/10.1061/jmcea3.0000969>
- Atkinson, G. M., & Boore, D. M. (2011). Modifications to Existing Ground-Motion Prediction Equations in Light of New Data. *Bulletin of the Seismological Society of America*, 101(3), 1121–1135. <https://doi.org/10.1785/0120100270>
- Atkinson, G. M., & Silva, W. (2000). Stochastic Modeling of California Ground Motions. *Bulletin of the Seismological Society of America*, 90(2), 255–274. <https://doi.org/10.1785/0119990064>
- Azar, S., Dabaghi, M., & Rezaeian, S. (2019). Probabilistic seismic hazard analysis using stochastic simulated ground motions. *Pubs.er.usgs.gov*. <https://doi.org/10.22725/ICASP13.235>
- Bahrapouri, M., Rodriguez-Marek, A., & Green, R. A. (2020). Ground motion prediction equations for Arias Intensity using the Kik-net database. *Earthquake Spectra*, 37(1), 428–448. <https://doi.org/10.1177/8755293020938815>
- Baker, J. W., Luco, N., Abrahamson, N. A., Graves, R. W., Maechling, P. J., and Olsen, K. B. Engineering uses of physics-based ground motion simulations. *Proceedings of the 10th National Conference in Earthquake Engineering, Earthquake Engineering Research Institute*, Anchorage, AK, 2014.

- Campbell, K. W., & Bozorgnia, Y. (2008). NGA Ground Motion Model for the Geometric Mean Horizontal Component of PGA, PGV, PGD and 5% Damped Linear Elastic Response Spectra for Periods Ranging from 0.01 to 10 s. *Earthquake Spectra*, 24(1), 139–171. <https://doi.org/10.1193/1.2857546>
- Campbell, K. W., & Bozorgnia, Y. (2014). NGA-West2 Ground Motion Model for the Average Horizontal Components of PGA, PGV, and 5% Damped Linear Acceleration Response Spectra. *Earthquake Spectra*, 30(3), 1087–1115. <https://doi.org/10.1193/062913eqs175m>
- Campbell, K. W., & Bozorgnia, Y. (2019). Ground Motion Models for the Horizontal Components of Arias Intensity (AI) and Cumulative Absolute Velocity (CAV) Using the NGA-West2 Database. *Earthquake Spectra*, 35(3), 1289–1310. <https://doi.org/10.1193/090818eqs212m>
- Chiou, Brian S.-J., & Youngs, R. R. (2008). An NGA Model for the Average Horizontal Component of Peak Ground Motion and Response Spectra. *Earthquake Spectra*, 24(1), 173–215. <https://doi.org/10.1193/1.2894832>
- Cui, Y., Olsen, K. B., Jordan, T. H., Lee, K., Zhou, J., Small, P., Roten, D., Ely, G., Panda, D. K., Chourasia, A., Levesque, J., Day, S. M., & Maechling, P. (2010). Scalable earthquake simulation on Petascale supercomputers. *2010 ACM/IEEE International Conference for High Performance Computing, Networking, Storage and Analysis*. <https://doi.org/10.1109/sc.2010.45>
- Dabaghi, M., & Der Kiureghian, A. (2018). Simulation of orthogonal horizontal components of near-fault ground motion for specified earthquake source and site characteristics. *Earthquake Engineering & Structural Dynamics*, 47(6), 1369–1393. <https://doi.org/10.1002/eqe.3021>
- Du, W., Ning, C. L., & Wang, G. (2019). The effect of amplitude scaling limits on conditional spectrum-based ground motion selection. *Earthquake Engineering & Structural Dynamics*, 48(9), 1030–1044. <https://doi.org/10.1002/eqe.3173>
- Eads, L., Hutt, C. M., & Menun, C. (2017). LOSS ASSESSMENT OF TALL BUILDINGS FROM A VULNERABILITY PERSPECTIVE. *16th World Conference on Earthquake Engineering*, 16WCEE 2017. Paper Number: 4869

- Faccioli, E., Bianchini, A., & Villani, M. (2010). New ground motion prediction equations for $T > 1$ s and their influence on seismic hazard assessment.
- Fayaz, J., Azar, S., Dabaghi, M., & Zareian, F. (2020). Methodology for Validation of Simulated Ground Motions for Seismic Response Assessment: Application to CyberShake Source-Based Ground Motions. *Bulletin of the Seismological Society of America*, 111(1), 226–241. <https://doi.org/10.1785/0120200240>
- Graves, R. W. (1996). Simulating Seismic Wave Propagation in 3D Elastic Media Using Staggered-Grid Finite Differences. *Bulletin of the Seismological Society of America*, 86(4), 1091–1106.
- Graves, R. W., & Pitarka, A. (2010). Broadband Ground-Motion Simulation Using a Hybrid Approach. *Bulletin of the Seismological Society of America*, 100(5A), 2095–2123. <https://doi.org/10.1785/0120100057>
- Graves, R., Jordan, T. H., Callaghan, S., Deelman, E., Field, E., Juve, G., Kesselman, C., Maechling, P., Mehta, G., Milner, K., Okaya, D., Small, P., & Vahi, K. (2010). CyberShake: A Physics-Based Seismic Hazard Model for Southern California. *Pure and Applied Geophysics*, 168(3–4), 367–381. <https://doi.org/10.1007/s00024-010-0161-6>
- Jones, P.S. (2010). Assessment of Performance Based Design Procedures for Tall Buildings. [Doctoral dissertation, University of California, Irvine]. ProQuest LLC.
- Jordan, T., Callaghan, S., Graves, R. W., Wang, F., Milner, K. R., Goulet, C. A., Maechling, P. J., Olsen, K. B., Cui, Y., Juve, G., Vahi, K., Yu, J., Deelman, E., & Gill, D. (2018). CyberShake Models of Seismic Hazards in Southern and Central California. *Proceedings of the 11th National Conference in Earthquake Engineering*.
- Kanno, T., Narita, A., Morikawa, N., Fujiwara, H., & Fukushima, Y. (2006). A New Attenuation Relation for Strong Ground Motion in Japan Based on Recorded Data. *Bulletin of the Seismological Society of America*, 96(3), 879–897. <https://doi.org/10.1785/0120050138>
- Karimzadeh, S., Askan, A., & Yakut, A. (2020). Evaluation of seismic performance measures for MDOF RC structures subjected to simulated and real ground motions. *MATEC Web of Conferences*, 323, 02003. <https://doi.org/10.1051/mateconf/202032302003>
- Kursa, M. B., Jankowski, A., & Rudnicki, W. R. (2010). Boruta – A System for Feature Selection. *Fundamenta Informaticae*, 101(4), 271–285. <https://doi.org/10.3233/fi-2010-288>

- Lee, E. J., Chen, P., & Jordan, T. H. (2014). Testing Waveform Predictions of 3D Velocity Models against Two Recent Los Angeles Earthquakes. *Seismological Research Letters*, 85(6), 1275–1284. <https://doi.org/10.1785/0220140093>
- Liu, P., Archuleta, R. J., & Hartzell, S. H. (2006). Prediction of Broadband Ground-Motion Time Histories: Hybrid Low/High-Frequency Method with Correlated Random Source Parameters. *Bulletin of the Seismological Society of America*, 96(6), 2118–2130. <https://doi.org/10.1785/0120060036>
- Mai, P. M., Imperatori, W., & Olsen, K. B. (2010). Hybrid Broadband Ground-Motion Simulations: Combining Long-Period Deterministic Synthetics with High-Frequency Multiple S-to-S Backscattering. *Bulletin of the Seismological Society of America*, 100(5A), 2124–2142. <https://doi.org/10.1785/0120080194>
- McVerry, G. H., Zhao, J. X., Abrahamson, N. A., & Somerville, P. G. (2006). New Zealand acceleration response spectrum attenuation relations for crustal and subduction zone earthquakes. *Bulletin of the New Zealand Society for Earthquake Engineering*, 39(1), 1–58. <https://doi.org/10.5459/bnzsee.39.1.1-58>
- Mena, B., Mai, P. M., Olsen, K. B., Purvance, M. D., & Brune, J. N. (2010). Hybrid Broadband Ground-Motion Simulation Using Scattering Green's Functions: Application to Large-Magnitude Events. *Bulletin of the Seismological Society of America*, 100(5A), 2143–2162. <https://doi.org/10.1785/0120080318>
- Moehle, J., Bozorgnia, Y., Jayaram, N., Jones, P., Rahnama, M., Shome, N., Tuna, Z., Wallace, J., Yang, T., & Zareian, F. (2011). Case Studies of the Seismic Performance of Tall Buildings Designed by Alternative Means. *Pacific Earthquake Engineering Research Center*. PEER Report 2011/05.
- Munjy, H., Habchi, R., & Zareian, F. (2021). Validation of simulated earthquake ground motions for displacement response of building and bridge structures based on intensity and frequency content parameters. *Journal of Structural Engineering*, 148(1). [https://doi.org/10.1061/\(asce\)st.1943-541x.0003212](https://doi.org/10.1061/(asce)st.1943-541x.0003212)
- Naeim, F. (2001). *The Seismic Design Handbook*. Springer.

- O'Brien, R. M. (2007). A Caution Regarding Rules of Thumb for Variance Inflation Factors. *Quality & Quantity*, 41(5), 673–690. <https://doi.org/10.1007/s11135-006-9018-6>
- Olsen, K. B., Day, S. M., Dalguer, L. A., Mayhew, J., Cui, Y., Zhu, J., Cruz-Atienza, V. M., Roten, D., Maechling, P., Jordan, T. H., Okaya, D., & Chourasia, A. (2009). ShakeOut-D: Ground motion estimates using an ensemble of large earthquakes on the southern San Andreas fault with spontaneous rupture propagation. *Geophysical Research Letters*, 36(4). <https://doi.org/10.1029/2008gl036832>
- Rezaeian, S., & Sun, X. (2014). Stochastic Ground Motion Simulation. *Encyclopedia of Earthquake Engineering*, 1–15. https://doi.org/10.1007/978-3-642-36197-5_239-1
- Rezaeian, S., Zhong, P., Hartzell, S., & Zareian, F. (2015). Validation of Simulated Earthquake Ground Motions Based on Evolution of Intensity and Frequency Content. *Bulletin of the Seismological Society of America*, 105(6), 3036–3049. <https://doi.org/10.1785/0120140210>
- Richards-Dinger, K., & Dieterich, J. H. (2012). RSQSim Earthquake Simulator. *Seismological Research Letters*, 83(6), 983–990. <https://doi.org/10.1785/0220120105>
- Schmedes, J., Archuleta, R. J., & Lavallée, D. (2010). Correlation of earthquake source parameters inferred from dynamic rupture simulations. *Journal of Geophysical Research*, 115(B3). <https://doi.org/10.1029/2009jb006689>
- Sebastiani, P. E., Liberatore, L., Lucchini, A., & Mollaioli, F. (2018). A new method to predict the critical incidence angle for buildings under near-fault motions. *Structural Engineering and Mechanics*, 68(5), 575–589. <https://doi.org/https://doi.org/10.12989/sem.2018.68.5.575>
- Sehhati, R., Rodriguez-Marek, A., ElGawady, M., & Cofer, W. F. (2011). Effects of near-fault ground motions and equivalent pulses on multi-story structures. *Engineering Structures*, 33(3), 767–779. <https://doi.org/10.1016/j.engstruct.2010.11.032>
- Selecting and Scaling Earthquake Ground Motions for Performing Response-History Analyses. *NEHRP Consultants Joint Venture*. NIST GCR 11-917-15
- Star, L. M., Stewart, J. P., & Graves, R. W. (2011). Comparison of Ground Motions from Hybrid Simulations to NGA Prediction Equations. *Earthquake Spectra*, 27(2), 331–350. <https://doi.org/10.1193/1.3583644>

- Teng, G., & Baker, J. (2019). Evaluation of SCEC CyberShake Ground Motions for Engineering Practice. *Earthquake Spectra*, 35(3), 1311–1328. <https://doi.org/10.1193/100918eqs230m>
- Zhong, Z. (2016). Ground Motion Simulation Validation for building design and response assessment. [Doctoral dissertation, University of California, Irvine]. University of California, Irvine, 2016. Print.